JAMES | Journal of Advances in Modeling Earth Systems

RESEARCH ARTICLE
10.1029/2018MS001596

Prognostic Precipitation in the MIROC6-SPRINTARS GCM: Description and Evaluation Against Satellite Observations

Takuro Michibata[1], Kentaroh Suzuki[2], Miho Sekiguchi[3], and Toshihiko Takemura[1]

[1]Research Institute for Applied Mechanics, Kyushu University, Fukuoka, Japan, [2]Atmosphere and Ocean Research Institute, University of Tokyo, Chiba, Japan, [3]Faculty of Marine Technology, Tokyo University of Marine Science and Technology, Tokyo, Japan

Key Points:
- Prognostic precipitation (both rain and snow) and its radiative effects are introduced into the MIROC6-SPRINTARS aerosol-climate model
- Aerosol-cloud-precipitation-climate interactions are evaluated using multisensor satellite data sets for different treatments of rain
- The radiative effect of snow is significant for both longwave and shortwave radiation and must be included for more reliable climate modeling

Correspondence to:
T. Michibata,
michibata@riam.kyushu-u.ac.jp

Citation:
Michibata, T., Suzuki, K., Sekiguchi, M., & Takemura, T. (2019). Prognostic precipitation in the MIROC6-SPRINTARS GCM: Description and evaluation against satellite observations. *Journal of Advances in Modeling Earth Systems*, *11*, 839–860. https://doi.org/10.1029/2018MS001596

Received 17 DEC 2018
Accepted 8 MAR 2019
Accepted article online 13 MAR 2019
Published online 29 MAR 2019

Abstract A comprehensive two-moment microphysics scheme is incorporated into the MIROC6-SPRINTARS general circulation model (GCM). The new scheme includes prognostic precipitation for both rain and snow and considers their radiative effects. To evaluate the impacts of applying different treatments of precipitation and the associated radiative effect, we perform climate simulations employing both the traditional diagnostic and new prognostic precipitation schemes, the latter also being tested with and without incorporating the radiative effect of snow. The prognostic precipitation, which maintains precipitation in the atmosphere across multiple time steps, models the ratio of accretion to autoconversion as being approximately an order of magnitude higher than that for the diagnostic scheme. Such changes in microphysical process rates tend to reduce the cloud water susceptibility as the autoconversion process is the only pathway through which aerosols can influence rain formation. The resultant anthropogenic aerosol effect is reduced by approximately 21% in the prognostic precipitation scheme. Modifications to the microphysical process rates also change the vertical distribution of hydrometeors in the manner that increases the fractional occurrence of single-layered warm clouds by 38%. The new scheme mitigates the excess of supercooled liquid water produced by the previous scheme and increases the total mass of ice hydrometeors. Both characteristics are consistent with CloudSat/CALIPSO retrievals. The radiative effect of snow is significant at both longwave and shortwave (6.4 and 5.1 W/m^2 in absolute values, respectively) and can alter the precipitation fields via energetic controls on precipitation. These results suggest that the prognostic precipitation scheme, with its radiative effects incorporated, makes an indispensable contribution to improving the reliability of climate modeling.

1. Introduction

Clouds and precipitation play significant roles in the global hydrological cycle and radiation budget. As such, appropriate representations of hydrometeor distributions are crucial for reliable climate simulation. The vertical distribution of precipitation is especially important because hydrometeors of different types and/or its phase (e.g., Matus & L'Ecuyer, 2017) have different sensitivities to the terrestrial and solar radiation spectra. In general circulation models (GCMs), however, the typical resolution of O(100 km) with ~30-min time step is not fine enough to capture individual cloud processes and subgrid-scale phenomena (e.g., Lebsock et al., 2013; Song et al., 2018a, 2018b), which must therefore be parameterized. For example, many GCMs treat precipitating hydrometeors (i.e., rain and snow) diagnostically, because the computational cost can be reduced by neglecting horizontal advection and by avoiding the restriction imposed by the Courant-Fredrichs-Levy (CFL) criteria on the vertical sedimentation of hydrometeors (see Gettelman & Morrison, 2015 for details), which is expedient for coarse resolution GCMs. On the other hand, such simplified representations can cause biases in both the microphysical and macrophysical aspects (e.g., Gettelman et al., 2013; Komurcu et al., 2014; Nam et al., 2012) due to the inherent lack of complexity in the modeled relationship between hydrometeors, the environment, and atmospheric dynamics (Stevens & Feingold, 2009; Wood, 2012).

Low-level clouds in the boundary layer are particularly likely to interact with aerosols. These interactions are referred to as "aerosol-cloud interactions" (ACI; Albrecht, 1989; Twomey, 1977) and are correlated with the environmental and thermodynamic conditions (Klein & Hartmann, 1993; Wood & Hartmann, 2006), whose complex morphology makes it difficult to emulate cloud system responses to aerosol perturbations (Bender

et al., 2018; Michibata et al., 2016; Sato et al., 2018; Zhou & Penner, 2017) in GCMs. This issue is manifested in the tendency for the magnitude of the ACI to be overestimated in GCMs (e.g., Quaas et al., 2009). Zhang et al. (2016) found a large spread among GCM simulations in the response of the liquid water path (LWP) to aerosol perturbations for different dynamic regimes, which implies that GCMs do not capture the regime dependence of aerosols on microphysics-dynamics interactions (Michibata et al., 2016; Wood, 2012).

The uncertainty in parameterizing cloud water susceptibility to aerosols is inextricably linked to uncertainty in rain formation. The cloud-to-rain water conversion in models is represented by the autoconversion process. The autoconversion rate is generally parameterized as a function of the cloud liquid water mixing ratio q_c and the cloud droplet number concentration N_c (e.g., Berry, 1968; Khairoutdinov & Kogan, 2000; Liu & Daum, 2004; Tripoli & Cotton, 1980) as

$$\left.\frac{\partial q_r}{\partial t}\right|_{\mathrm{aut}} = C_{\mathrm{aut}}\, q_c^{\alpha} N_c^{-\beta}. \tag{1}$$

Likewise, accretion of cloud droplets by raindrops is generally parameterized as a function of the q_c and rainwater mixing ratio q_r (e.g., Michibata & Takemura, 2015; Wu et al., 2018) as

$$\left.\frac{\partial q_r}{\partial t}\right|_{\mathrm{acc}} = C_{\mathrm{acc}}\,(q_c q_r)^{\gamma}\ , \tag{2}$$

where C_{aut}, C_{acc}, α, β, and γ are the prescribed constants. The increased N_c, due to increased aerosol concentration, decreases the autoconversion rate, prolonging the cloud lifetime. As a result, the cloud-to-rain microphysical transition is highly sensitive to the autoconversion scheme used (Suzuki et al., 2013a; Wood, 2005a).

Suzuki et al. (2015) evaluated the rain formation process by comparing outputs from a multimodel analysis (using both GCMs and a cloud-resolving model, CRM) with satellite observations. The GCMs were found to simulate rain formation too early, even in the case of smaller cloud droplets with size <10 μm, where drizzle initiation rarely occurs (e.g., Michibata et al., 2014; Nakajima et al., 2010a; Suzuki et al., 2011). On the other hand, only the CRM could satisfactorily capture the cloud-to-rain transition process observed in the satellite data. One of the causes of this systematic difference could be attributed to the treatment of precipitation in the model (Takahashi et al., 2017; Wang et al., 2012), that is, diagnostic (hereinafter "DIAG") and prognostic (hereinafter "PROG") approaches. For example, although small drizzle drops, which do not reach the surface within a single-model time step, are suspended in the real atmosphere (e.g., Wood, 2012), the DIAG method assumes that all the diagnosed rainwater precipitates to the surface within a single time step. This introduces biases in precipitation frequency and/or intensity (Stephens et al., 2010) as well as in the radiative properties (Michibata & Takemura, 2015).

It is also worth noting that there is a critical discrepancy between the "process-oriented constraints" of microphysics, deduced from satellite data (Suzuki et al., 2013b), and the "performance-oriented constraints" of the climate trend used for empirical model tuning (Golaz et al., 2013). This discrepancy is accounted for by means of error compensation in the model parameterization and in the historical temperature trend via the arbitrary "tunable knobs" in GCMs (Suzuki et al., 2013b). Recent work performed by Mulcahy et al. (2018) improved the estimates of effective radiative forcing by updating aerosol processes, such as the cloud droplet spectral dispersion, aerosol activation scheme, and black carbon optical property. These studies strongly assert that the modeling framework used to depict aerosol-cloud-precipitation interactions must be developed at the fundamental process level toward a more physically representative parameterization (Seinfeld et al., 2016).

In terms of solid precipitation process, snowflakes fall from higher altitudes with slower fall velocities than raindrops and are thus characterized by longer residence time. The representation issues that arise when using the DIAG scheme are therefore critical for the warm rain microphysics discussed above and for approximating the vertical distribution of solid hydrometeors (Reitter et al., 2011). For example, Waliser et al. (2009) showed that the larger-sized precipitating ice (i.e., snow and graupel) will account for more than 60% of the total ice water path (TIWP) retrieved from the CloudSat radar measurement. However, the DIAG parameterization fundamentally misses the precipitating hydrometeors in the atmosphere, further generating biases in the radiation field (Li et al., 2014; Waliser et al., 2011). Li et al. (2014) investigated the impact of the snow radiative effect by conducting sensitivity experiments with and without snow in their radiative transfer computations. They emphasized the significance of the radiative effect of snow, which alters

atmospheric circulation via cloud-radiation-dynamics interactions and which may also mitigate biases in the land surface temperature (Li et al., 2016).

In this situation, advanced frameworks for cloud precipitation microphysics, such as the prognostic precipitation scheme, have recently been introduced into GCMs to improve representation of the microphysics and hydrometeor distribution (Gettelman et al., 2015; Sant et al., 2015; Walters et al., 2011). It was found that representation of the proportion of microphysical processes, denoted by the accretion-to-autoconversion ratio (Acc/Aut), was significantly improved when compared with in situ measurements (Gettelman et al., 2013; Wood et al., 2011), due to enhancement of the accretion process (Posselt & Lohmann, 2008). The enhancement in the Acc/Aut ratio results in relaxation of the aerosol forcing (Posselt & Lohmann, 2009), since the aerosol effect depends only on the autoconversion process via its relationship with N_c as described in equation (1) whereas the accretion process is independent of aerosol (or cloud droplet) numbers as described in equation (2).

Motivated by these successful studies, we develop a comprehensive two-moment microphysics scheme based on a prognostic precipitation framework (incorporating both rain and snow) for an aerosol-climate model, the MIROC6-SPRINTARS GCM. The new framework includes a radiation calculation for prognostic hydrometeors. The main objective of our study is to clarify how different treatments of precipitation (i.e., DIAG vs. PROG) in GCMs will impact on microphysical processes, the distribution of hydrometeors, and radiative forcing on the climate system. The model configurations between the two versions are the same except for the treatment of precipitation, and simulations are conducted under the same tuning parameters, in order to isolate the role of the precipitation framework as much as possible (cf. section 2). The performance and advantages of the PROG scheme relative to the traditional DIAG scheme are evaluated in comparison with multisensor satellite measurements. In section 2, we describe the model, summarize the new microphysics scheme, and detail the relevant updates in MIROC6. In section 3 we present our results and discussion. Our conclusions and plans for future work are summarized in section 4.

2. Model and Methods

2.1. General Model Description

We employ the latest (sixth) version of the Model for Interdisciplinary Research on Climate (MIROC) in this study. The SPRINTARS (Spectral Radiation-Transport Model for Aerosol Species) aerosol module, which simulates global transport of the major species of tropospheric aerosols (Takemura et al., 2000, 2002, 2005), is coupled with MIROC6 (Tatebe et al., 2019). SPRINTARS prognoses the mass-mixing ratios of carbonaceous aerosols (black carbon and organic matter), sea salt, soil dust, and sulfate. The precursor gases of sulfate, that is, sulfur dioxide and dimethyl sulfide, and organic matter (terpene and isoprene) are also considered explicitly. The aerosol transport processes treated include emission, advection, diffusion, the chemical reaction of sulfate and organic matter, dry and wet deposition, and gravitational settling.

MIROC6 introduces shallow cumulus parameterization (Park & Bretherton, 2009) to reduce the dry bias in the free troposphere found in MIROC5 over low-latitude oceans. The treatment of cloud microphysics and planetary boundary layer schemes in MIROC6 is the same as in the previous version, MIROC5 (see Tatebe et al., 2019, for a detailed comparison between MIROC5 and 6). MIROC6 incorporates a probability density function (PDF) based prognostic large-scale condensation scheme, which parameterizes explicitly for subgrid-scale cloud variability (Watanabe et al., 2009). This scheme assumes small fluctuations in the total water-mixing ratio q_t within the model grid and predicts variance and skewness of the PDF ($G(q_t)$). Cloud is formed for the fraction of the model grid where q_t exceeds supersaturation q_{sat} with respect to liquid. The PDF shape is characterized by a triangular basis function, which varies depending on cloud microphysics, cumulus convection, turbulent mixing, and advection. The cloud fraction (CF) and liquid water mixing ratio are thus computed by integrating the PDF over the saturated pixels in the model grid as,

$$\mathrm{CF} = \int_{q_{\mathrm{sat}}}^{\infty} \mathrm{G}(q_t)\,\mathrm{d}q_t \tag{3}$$

and

$$\overline{q_c} = \int_{q_{\mathrm{sat}}}^{\infty} (q_t - q_{\mathrm{sat}}) \cdot \mathrm{G}(q_t)\,\mathrm{d}q_t\ , \tag{4}$$

respectively, where $\overline{q_c}$ denotes the grid mean value.

The PDF scheme is coupled to the ice microphysics scheme based on Wilson and Ballard (1999), which solves homogeneous and heterogeneous nucleation, deposition, sublimation, riming, and ice melt. MIROC-SPRINTARS employs a two-moment bulk cloud microphysics scheme for both liquid droplets and ice crystals, the formulations for which are documented in Takemura et al. (2009). The nucleation of cloud droplets from aerosols is based on Abdul-Razzak and Ghan (2000).

The cloud-to-rain conversion is diagnosed from Berry (1968) scheme. The standard version of MIROC6 treats both rain and snow diagnostically and assumes that the precipitating hydrometeors diagnosed at the present time step fall to the surface instantaneously (Ghan & Easter, 1992). This approach is reasonable for relatively large hydrometeors with fall velocities in the range 3–5 m/s, and which fall 1,800–6,000 m in the typical time step applied in GCMs of 10–20 min. The DIAG approach is not constrained by the CFL condition in the sedimentation process of precipitating hydrometeors, which is convenient for GCMs with long time steps as it reduces the computational cost. However, the DIAG method neglects small raindrops and/or snowflakes with residence times longer than the model time step. This introduces further biases in the hydrological cycle and vertical distribution of hydrometeors as well as in the resulting radiation field since the errors in sedimentation of precipitating hydrometeors can further lead to biases in the evaporation (sublimation) of raindrops (snowflakes), which can also influence thermal transport due to these processes.

2.2. Prognostic Precipitation Framework

We have significantly reconstructed the default DIAG rain scheme in the MIROC6-SPRINTARS setup described above for both liquid and solid precipitation processes. The new scheme includes prognostic precipitation based on the two-moment approach, which solves prognostic equations for both mass (denoted as q) and number (denoted as N) mixing ratios with regard to the rain (q_r and N_r) and snow (q_s and N_s) bulk categories. The associated time tendencies are described as

$$\frac{\partial q_x}{\partial t} = -\frac{1}{\rho_a}\nabla\cdot(\rho_a \mathbf{u} q_x) - \frac{1}{\rho_a}\frac{\partial(\rho_a q_x v_{q_x})}{\partial z} + S_{q_x} \quad \text{and} \tag{5}$$

$$\frac{\partial N_x}{\partial t} = -\frac{1}{\rho_a}\nabla\cdot(\rho_a \mathbf{u} N_x) - \frac{1}{\rho_a}\frac{\partial(\rho_a N_x v_{N_x})}{\partial z} + S_{N_x}\,, \tag{6}$$

where $x \in \{r \text{ and } s\}$, ρ_a is the air density, and $\mathbf{u}$ is the wind vector. The v_{q_x} and v_{N_x} are the bulk fall velocities, weighted by mass and number, respectively, and are described in greater detail later (cf. equations (10), (11), (14), and (15)). The S_{q_x} and S_{N_x} are the source/sink of the mass and number mixing ratios with respect to condensation, evaporation, and other microphysical collection processes (e.g., autoconversion, accretion, and self-collection). These "conservation equations" are newly introduced into MIROC6-SPRINTARS, and now the cloud microphysics and macrophysics link synchronously with precipitation. Convective cumulus is still treated diagnostically.

Table 1 summarizes the microphysical processes considered in the new PROG framework, called CHIMERRA (Cloud/Hydrometeors Interactive Module with Explicit Rain and Radiation). We have updated the autoconversion and accretion schemes based on Khairoutdinov and Kogan (2000). This scheme assumes the initial size of a raindrop to be 25 μm, allowing for the rain class to include drizzle. Self-collection among raindrops is represented following the method described by Beheng (1994). Within the ice microphysics component, ice-to-snow aggregation is based on the Morrison and Gettelman (2008) scheme, which represents snow by converting cloud ice that has been identified as exceeding the critical threshold size over the conversion timescale. Cloud droplets, ice crystals, and raindrops are accreted by snowflakes, which are parameterized using the Seifert and Beheng (2006) and Reisner et al. (1998) methods. The dominant source term for cloud ice and snow is Bergeron-Findeisen (BF) process (Bergeron, 1935; Findeisen, 1938), which is parameterized according to the Rotstayn et al. (2000) scheme. We do not apply any upper or lower thresholds for either the mass or number mixing ratios of precipitating hydrometeors. Instead, raindrops or snowflakes break up when their mean diameter exceeds 2 or 4 mm, respectively. Such cases are rare in our simulations.

The above microphysical processes are calculated within each subtime step (60 s in this study). Model performance is highly sensitive to the duration of the subtime step used (Posselt & Lohmann, 2008), which is correlated with the nonlinear representation of microphysical process rates such as the autoconversion and accretion terms (see Gettelman et al., 2015 for details). Fewer substeps can cause errors in representing the sedimentation process, which, in turn, influences the evaporation and sublimation of precipitation. The

Table 1
Summary of Interaction Processes Among Hydrometeors (Water Vapor "v", Liquid Cloud "c", Cloud Ice "i", Rain "r", and Snow "s") for Mass (q) and Number (N) Implemented in the New Prognostic Precipitation Framework

Process	Interaction	q_c	q_i	q_r	q_s	N_c	N_i	N_r	N_s	References
Prognostic rain										
Autoconversion	c + c → r	↓		↑		↓		↑		Khairoutdinov and Kogan (2000)
Accretion	c + r → r	↓		↑		↓				Khairoutdinov and Kogan (2000)
Self-collection	r + r → r							↓		Beheng (1994)
Evaporation	r → v			↓				↓		Khairoutdinov and Kogan (2000)
Sedimentation	r			↑↓				↑↓		Sant et al. (2015)
Breakup	r → r							↑		
Prognostic snow										
Instantaneous melt	s → r			↑	↓			↑	↓	
Freezing of rain	r → s			↓	↑			↓	↑	
Aggregation	i + i → s		↓		↑		↓		↑	Morrison and Gettelman (2008)
Accretion	c + s → s	↓			↑	↓				Seifert and Beheng (2006)
	i + s → s		↓		↑		↓			Seifert and Beheng (2006)
	r + s → s			↓	↑			↓		Reisner et al. (1998)
Hallet-Mossop	c → i	↓	↑				↑			Cotton et al. (1986)
Self-aggregation	s → s								↓	Passarelli (1978)
Sublimation	s → v				↓				↓	Rotstayn et al. (2000)
Sedimentation	s				↑↓				↑↓	Sant et al. (2015)
Bergeron	c → i	↓	↑							Rotstayn et al. (2000)
	c → s	↓			↑					Gettelman and Morrison (2015)
Breakup	s → s								↑	

Note. The up (down) arrows indicate that the process leads to an increase (decrease) in mass and number-mixing ratios.

iteration with regard to the sedimentation of hydrometeors can be shorter dependent on the vertical CFL criteria, as described in more detail later.

The subgrid precipitation fraction is determined by assuming the maximum cloud overlap, which neglects a possible tilting of precipitation shafts between the two adjacent levels. We also assume that the precipitation occurs uniformly in the cloudy area, without considering in-cloud precipitation inhomogeneity (see also detailed description of other methods in Chosson et al., 2014 and Turner et al., 2012). The model does not take into account horizontal advection of the precipitation fraction.

The raindrop size distribution $N(D)$ is based on the modified gamma distribution (Ulbrich, 1983), described as

$$N(D) = \frac{N_x}{\Gamma(\mu_x)} \left(\frac{D}{D_{0,x}} \right)^{\mu_x} \frac{1}{D} \exp\left(-\frac{D}{D_{0,x}} \right) , \tag{7}$$

where $\Gamma(\mu_x)$ is the Gamma function, and N_x and D are the total number concentration (m^{-3}) and the diameter of the hydrometeor (m), respectively. $N(D)$ depends on both the shape parameter μ_x and the distribution parameter $D_{0,x}$, calculated as

$$D_{0,x} = \frac{\bar{D}_x}{\sqrt[3]{(\mu_x + 2)(\mu_x + 1)\mu_x}} , \tag{8}$$

where the mean diameter of the hydrometeor $\bar{D}_x$ (m) is

$$\bar{D}_x = \sqrt[3]{\frac{6}{\pi \rho_w} \frac{\rho_a q_x}{N_x}}. \tag{9}$$

Where ρ_w is the density of water, assumed to be 1,000 kg/m^3. For snowflakes, ρ_s is assumed to be 250 kg/m^3 in our model.

For the rain class, the mass and number weighted bulk fall velocities, v_{q_r} and v_{N_r}, are approximated based on Rogers et al. (1993), and are described as follows (Posselt & Lohmann, 2009; Sant et al., 2015):

$$v_{q_r} = \begin{cases} (\mu_r + 3) b_v D_{0,r} & \text{for } D_{0,r} < D_v/(\mu_r + 3) \\ b_1 & \text{for } D_{0,r} > D_v/(\mu_r + 3) \end{cases}, \tag{10}$$

$$v_{N_r} = \begin{cases} \mu_r b_v D_{0,r} & \text{for } D_{0,r} < D_v/\mu_r \\ b_1 & \text{for } D_{0,r} > D_v/\mu_r \end{cases}, \tag{11}$$

with the constants $b_1 = 9.65$ m/s, $b_v = 3{,}918\ s^{-1}$, and $D_v = 2{,}463\ \mu$m. Thus, the sedimentation of the mixing ratios in flux form is expressed as

$$\left.\frac{\partial q_r}{\partial t}\right|_{\text{sed}} = \frac{1}{\rho_a}\frac{\partial}{\partial z}(\rho_a q_r v_{q_r}), \tag{12}$$

$$\left.\frac{\partial N_r}{\partial t}\right|_{\text{sed}} = \frac{1}{\rho_a}\frac{\partial}{\partial z}(\rho_a N_r v_{N_r}), \tag{13}$$

which are strictly constrained by the CFL criteria in the vertical, such that $C = v_{q_x}\Delta t/\Delta z < 1$ will be satisfied. Although we apply the classic Euler forward scheme to solve the sedimentation of falling hydrometeors using subtime stepping described above, prognostic approaches also can avoid the CFL constraints by applying semi-Lagrangian method (e.g., Juang & Hong, 2010; Staniforth & Cote, 1991; Xiao et al., 2003), or box-Lagrangian scheme (Kato, 1995), or exponential limiters (Rotstayn, 1997). It is worth investigating in future studies how the computational efficiency and the modeled climatology are sensitive to the different types of sedimentation scheme.

For the snow class, mass and number weighted fall velocities are described as

$$v_{q_s} = \beta_1 D_{0,s}^{\beta_2} \frac{\Gamma(\mu_s + 3 + \beta_2)}{\Gamma(\mu_s + 3)}, \tag{14}$$

$$v_{N_s} = \beta_1 D_{0,s}^{\beta_2} \frac{\Gamma(\mu_s + \beta_2)}{\Gamma(\mu_s)}, \tag{15}$$

where β_1 and β_2 are characterized by the particle types and riming degree (Barthazy & Schefold, 2006) and are chosen to be consistent with the particle types categorized within the radiation module in MIROC6, described in more detail later (cf. section 2.3). The shape parameters for rain and snow are prescribed as $\mu_r = 5$ and $\mu_s = 1$, respectively, for the consistency with previous work by Sant et al. (2015).

2.3. Radiation Calculation for Precipitating Hydrometeors

The radiative transfer in MIROC6-SPRINTARS is solved using mstrnX (Sekiguchi & Nakajima, 2008), which is a *k*-distribution based two-stream approximation radiative transfer package. The mstrnX used in this study discretizes 29 spectral bands for the radiative transfer calculation, of which 15 are solar and 14 are thermal.

For hydrometeors, the mstrnX considers liquid droplets within the range 1 to 200 μm, and ice crystals (and snowflakes for the PROG scheme) within the range 5 to 500 μm. In the PROG scheme, raindrops are also considered within the radiation calculation, but their effect is small (e.g., Hill et al., 2018). Solid hydrometeors are considered as hexagonal columns in the cloud ice bulk category and as dendrite crystals in the snow category. The scattering, absorption, and polarization properties of solid hydrometeors are based on Yang et al. (2013). With the exception of precipitating hydrometeors, the radiation table employed in the DIAG and PROG schemes is the same.

2.4. Experimental Design and Model Setup

We performed sets of simulations using both the DIAG and PROG schemes with present-day (PD) and preindustrial (PI) emissions to investigate aerosol-cloud interactions. For the PD experiment, the emission inventories used for black carbon, organic carbon, and sulfur dioxide are sourced from the Global Fire Emissions Database (GFED) version 3.1, based on biomass burning (Randerson et al., 2013), and the Hemispheric Transport of Air Pollution (HTAP) Phase 2 data, representing anthropogenic sources (Janssens-Maenhout et al., 2012). The monthly oxide fields of O_3, OH, and H_2O_2 are based on RCP historical emission data.

Table 2
Global Annual Mean Values From the DIAG and PROG Schemes With and Without Snow Radiation Simulation

	DIAG	PROG ON/SnwRad	PROG OFF/SnwRad	Reference value and source
Autoconversion rate ($kg \cdot m^{-2} \cdot s^{-1}$)	9.1×10^{-6}	1.8×10^{-6}	1.8×10^{-6}	—
Accretion rate ($kg \cdot m^{-2} \cdot s^{-1}$)	3.9×10^{-6}	6.2×10^{-6}	6.2×10^{-6}	—
Acc/Aut ratio	0.14	4.62	4.67	1–100 (VOCALS: Gettelman et al., 2013)
CLWP (g/m^2)	94.3	89.2	86.7	84.7 (SSMIS F16)
CIWP (g/m^2)	28.6	6.2	6.3	23.0–26.7 (CloudSat: Li et al., 2012)
RWP (g/m^2)	–	25.7	25.3	—
SWP (g/m^2)	–	86.0	82.3	—
N_c burden (10^{10} m^{-2})	1.6	1.0	0.9	—
N_i burden (10^8 m^{-2})	50	2.5	2.5	—
N_r burden (10^7 m^{-2})	–	4.2	4.0	—
N_s burden (10^7 m^{-2})	–	6.2	6.1	—
Precipitation rate (mm/day)	3.25	3.03	3.13	2.67 (GPCP v2.2)
Total cloud cover (%)	55.8	59.1	58.4	65.4 (ISCCP D2), 67.2 (CALIPSO-GOCCP)
High cloud cover (%)	23.2	25.5	25.1	32.9 (CALIPSO-GOCCP)
Middle cloud cover (%)	9.2	9.5	9.9	18.3 (CALIPSO-GOCCP)
Low cloud cover (%)	25.7	26.6	26.0	37.4 (CALIPSO-GOCCP)
COT	10.6	9.7	9.4	13.1 (MODIS C6)
CER (μm)	11.9	10.0	9.9	13.8 (MODIS C6)
AOT	0.108	0.097	0.092	0.160 (MODIS C6)
OLR (W/m^2)	237.2	237.3	243.7	240.3 (CERES EBAF–TOA radiation Ed4.0)
OSR (W/m^2)	−237.5	−236.8	−241.9	−241.2 (CERES EBAF–TOA radiation Ed4.0)
LWCRF (W/m^2)	25.2	23.7	16.5	28.0 (CERES EBAF–TOA radiation Ed4.0)
SWCRF (W/m^2)	−51.1	−52.6	−47.0	−45.8 (CERES EBAF–TOA radiation Ed4.0)
NetCRF (W/m^2)	−26.0	−28.9	−30.5	−17.8 (CERES EBAF–TOA radiation Ed4.0)

Note. In the case of reference values taken from previous studies, the reference paper is specified in the list. The satellite data products for comparison with the model outputs were obtained from the following: Special Sensor Microwave Imager Sounder (SSMIS) F16 (Wentz et al., 2012) for liquid water path (LWP) for the period 2006–2010; Global Precipitation Climatology Project (GPCP) version 2.2 (Adler et al., 2003) for precipitation rate for the period 2001–2013; International Satellite Cloud Climatology Project (ISCCP) D2 data set (Rossow & Schiffer, 1999) and CALIPSO General Circulation Model-Oriented CALIPSO Cloud Product (CALIPSO-GOCCP) version 3.1.2 (Chepfer et al., 2010) for cloud cover for the periods 2005–2009 and 2006–2017, respectively; Aqua-Moderate Resolution Imaging Spectroradiometer (MODIS) C6 level-3 monthly product (Platnick et al., 2017) for cloud optical thickness (COT), cloud droplet effective radius at the cloud top (CER), and aerosol optical thickness (AOT) for the period 2006–2010; CERES EBAF-TOA Edition 4.0 (Loeb et al., 2018) for longwave and shortwave radiation and cloud radiative forcing (OLR, OSR, LWCRF, and SWCRF) at the top of the atmosphere (TOA) for the period 2001–2017.

We conducted simulations, using prescribed climatological sea surface temperature, over 6-year period, with the last 5 years being used in the subsequent analysis. The model resolution is T85 (approximately 1.4° resolution in longitude and latitude) with 40 vertical levels. The standard time step is 12 min, which becomes shorter in cases with unstable conditions.

Another sensitivity experiment was performed in which the radiative effect of snow was turned off to investigate the radiative impact of snow. The majority of GCMs continue to ignore snow's radiative effect (Li et al., 2012; Waliser et al., 2011) due to their diagnostic treatment of precipitation. Simulations with and without snow radiation (hereinafter, ON/SnwRad and OFF/SnwRad) were carried out with the aim of understanding the importance of this parameter in GCMs. The results are discussed in section 3.4.

3. Results and Discussion

3.1. Global Statistics

The global annual mean values from three types of simulations and reference values are summarized in Table 2. Although most of the reference values analyzed in this study are taken from observations, the

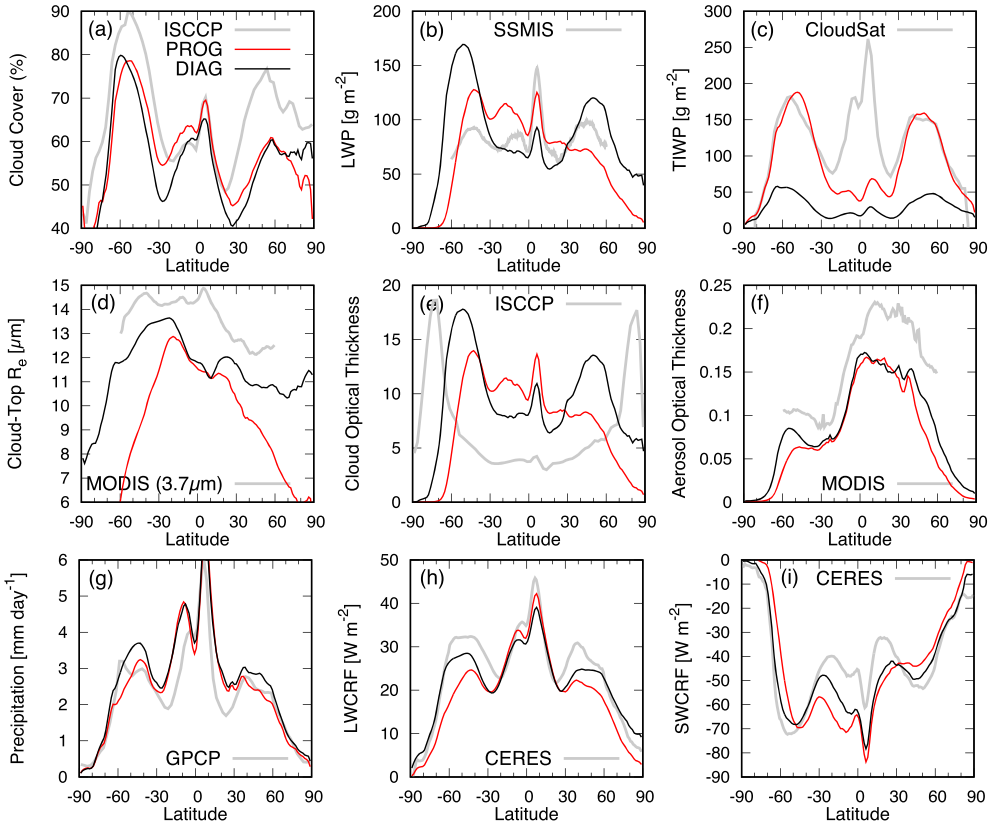

Figure 1. Zonal mean (a) total cloud cover, (b) liquid water path, (c) total ice water path (i.e., CIWP + SWP), (d) liquid cloud top effective radius, (e) cloud optical thickness, (f) aerosol optical thickness, (g) precipitation rate, (h) longwave cloud radiative forcing, and (i) shortwave cloud radiative forcing, for DIAG (black) and PROG (red) simulations. Observational data from ISCCP D2 (for the period 2005–2009), SSMIS/F16 (2006–2010), CloudSat and CALIPSO 2C-ICE product (2006–2011), Aqua-MODIS Level 3 (2006–2010), GPCP version 2.2 (2001–2013), and CERES EBAF–TOA Ed4.0 (2001–2017) are also plotted (gray) for reference. ISCCP = International Satellite Cloud Climatology Project; PROG = prognostic; DIAG = diagnostic; SSMIS = Special Sensor Microwave Imager Sounder; MODIS = Moderate Resolution Imaging Spectroradiometer; GPCP = Global Precipitation Climatology Project.

values cited for some unavailable parameters are from previous studies or other models, for which the corresponding references have been specified.

As we expected, the process rates, that is, the autoconversion and accretion rates, are altered significantly when switching between the DIAG and PROG schemes. Within the PROG framework, the prognosed rainwater is stored in the atmosphere across multiple time steps, enhancing the accretion rate. The Acc/Aut ratio is approximately an order of magnitude higher in the PROG implementation than in the traditional DIAG scheme, and is in closer agreement with the VOCALS in situ aircraft measurements (Gettelman et al., 2013; Wood et al., 2011) as well as with results from previous modeling studies (Gettelman & Morrison, 2015; Sant et al., 2015). Note that the Acc/Aut ratio is calculated locally using instantaneous process rates, and then the ratio averaged vertically over the entire cloud layer. The Acc/Aut ratio is fundamentally related to the magnitude of aerosol-cloud interactions because aerosol (or N_c) modifies the autoconversion rate but not the accretion rate (see equations (1) and (2)). We further discuss the links between microphysical processes and aerosol-cloud interactions in later sections (cf. sections 3.2 and 3.3). Implementation of the PROG ON/SnwRad and PROG OFF/SnwRad settings results in comparable outputs, with the exception of the radiation field and derived precipitation.

The PROG scheme decreases the cloud liquid water path (CLWP) slightly more so than the DIAG scheme as some liquid water shifts to the rain class and remains in the atmosphere. However, this does not correspond directly to changes in cloud fraction. The total cloud amount increases by 3.3–3.6% in the PROG scheme, with contributions of additional low- (~1%) and high-level cloud (~2%). However, the total cloud amount is still less than that observed, especially over midlatitudes (Figure 1a).

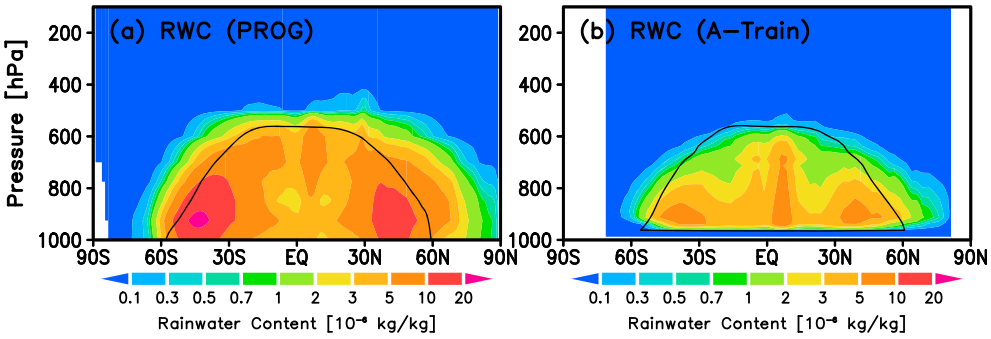

Figure 2. Zonal mean distribution of rainwater mass mixing ratio for (a) MIROC6 with PROG scheme and (b) CloudSat radar retrieval from the 2C-RAIN-PROFILE product. The black line indicates a guide for the annual zonal mean melting level at $T = 273$ K from (a) the intrinsic model value and (b) the ECMWF-AUX product. Note that the model only includes stratiform clouds (see text for details). CloudSat retrieval misses near-surface hydrometeors (below ~1 km) due to ground clutter contamination. RWC = rainwater content; PROG = prognostic.

Figure 2 shows a vertical cross section of rainwater content for a MIROC6 PROG simulation and CloudSat radar retrieval (2C-RAIN-PROFILE product; Lebsock et al., 2011) with the ECMWF-AUX product (Partain, 2007). Note that the CloudSat retrieval misses near-surface rainwater (below ~1 km) due to ground clutter contamination (Marchand et al., 2008; Tanelli et al., 2008). CloudSat observations show high rainwater mass over midlatitude areas at lower altitude, just below the melting line. This detail is well reproduced within the model. Such observations can be attributed to long-lived smaller drizzle drops, and/or contributions from melting snow. We do not compare the absolute value of the rainwater in the atmosphere because the observations can include bias in rainwater retrieval due to radar attenuation and the detection sensitivity of the cloud profiling radar (Stephens et al., 2008).

In the PROG simulation, cloud liquid water content above the melting layer is significantly reduced, which is realistic when compared with the CloudSat observations (Figures 3a–3c). For the ice phase, the cloud ice water path (CIWP) is reduced in PROG while the snow water path (SWP) is explicitly preserved across multiple time steps, and hence the total ice water path (TIWP = CIWP + SWP) is significantly higher in the PROG simulation and is in good agreement with CloudSat and CALIPSO retrievals (Figures 3d–3f). The reason for this systematic difference between PROG and DIAG is that parameterization of the depositional growth of

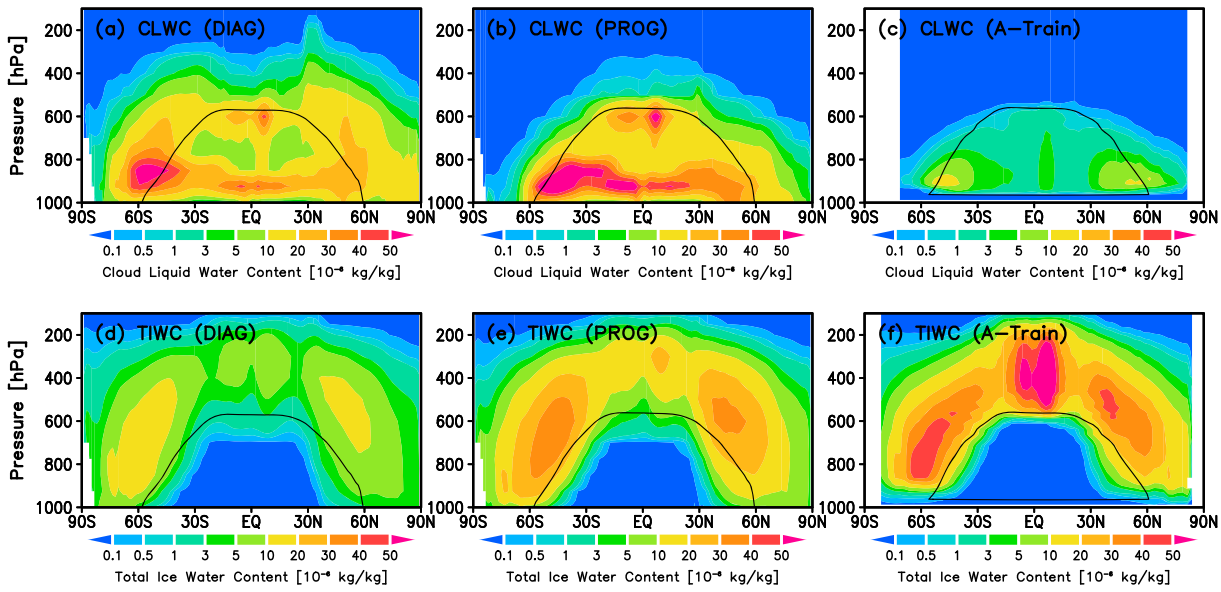

Figure 3. Zonal mean distribution of (top row) cloud liquid and (bottom row) total ice mass mixing ratios for (a, d) MIROC6 DIAG scheme, (b, e) PROG scheme, and (c, f) CloudSat and CALIPSO satellite retrievals. CLWC= cloud liquid water content; DIAG = diagnostic; PROG = prognostic; TIWC = total ice water content.

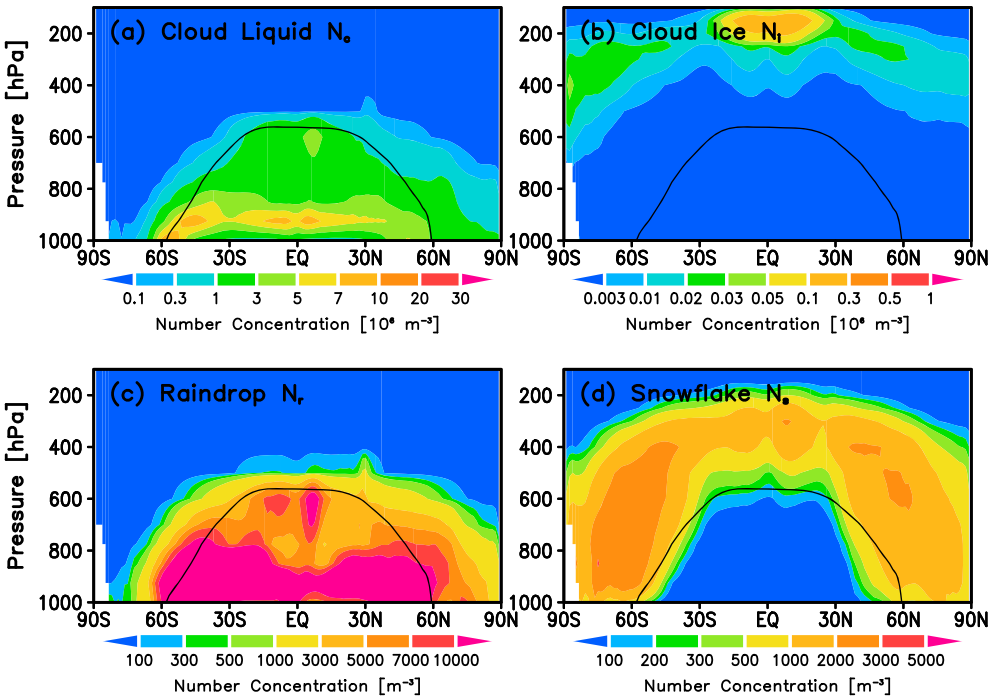

Figure 4. Zonal mean distribution of number mixing ratios simulated in the MIROC6 PROG scheme for (a) N_c, (b) N_i, (c) N_r, and (d) N_s.

ice hydrometeors is more efficient due to the BF process in the PROG (not shown), which depletes coexisting supercooled liquid water (Fan et al., 2011; Rotstayn et al., 2000). It is interesting to note that the liquid water content at lower altitude (>800 hPa) is increased in the PROG scheme even though the global mean CLWP is reduced relative to that derived within the DIAG scheme (Figures 3a and 3b, and Table 2). We further investigated the instantaneous output and found that the occurrence frequency of single-layered warm clouds is increased by ~38% in the PROG scheme, whereas the horizontal distribution is approximately the same for the two schemes (not shown). Changes in the vertical distribution of hydrometeors (i.e., the phase) will further affect cloud feedback (Matus & L'Ecuyer, 2017) and model climate sensitivity (e.g., Gettelman & Sherwood, 2016; McCoy et al., 2016; Tan et al., 2016). This will be addressed further in future work.

As a result, both the liquid- and ice-column path representations show considerable improvement in the PROG scheme (Figures 1b, 1c, 2, and 3) when compared with the DIAG scheme. TIWP remains underestimated over the tropics (Figures 1c and 3e) because the precipitation (rain and snow) prognosed in the model is only representative for large-scale contributions, but not for convective clouds. As shown in Table 2 and Figure 4, the number concentrations of each hydrometeor in the PROG scheme are consistent with the findings of Wang et al. (2011), based on a multiscale modeling framework with an embedded cloud-resolving model (PNNL-MMF).

The PROG scheme does not always lead to improvements in the representation of microphysics parameters such as the cloud droplet effective radius (CER), the cloud optical thickness (COT), and the aerosol optical thickness (AOT; see Figures 1d–1f). We obtained MODIS-CER retrievals from the 3.7 μm band (not from the 2.1 μm band) to effectively represent the upper cloud top property (e.g., Nakajima et al., 2010b; Platnick, 2000). MIROC6 underestimates the CER compared with the MODIS satellite retrieval, resulting in brighter COT in liquid clouds (Figures 1d and 1e). These results suggest that the so-called "too few too bright low cloud problem" (Calisto et al., 2014; Nam et al., 2012) remains an unresolved issue in MIROC6, although the microphysical parameters also have large retrieval uncertainties (e.g., King et al., 2013; Merk et al., 2016; Zhang et al., 2012). A further study using satellite simulators (Bodas-Salcedo et al., 2011; Swales et al., 2018) is desired, but is beyond the scope of this paper.

AOT is decreased by ~10% in the PROG simulation relative to the DIAG scheme, mainly at midlatitudes (Figure 1f), due to enhancement of wet scavenging, associated with the prognostic treatment of precipitation

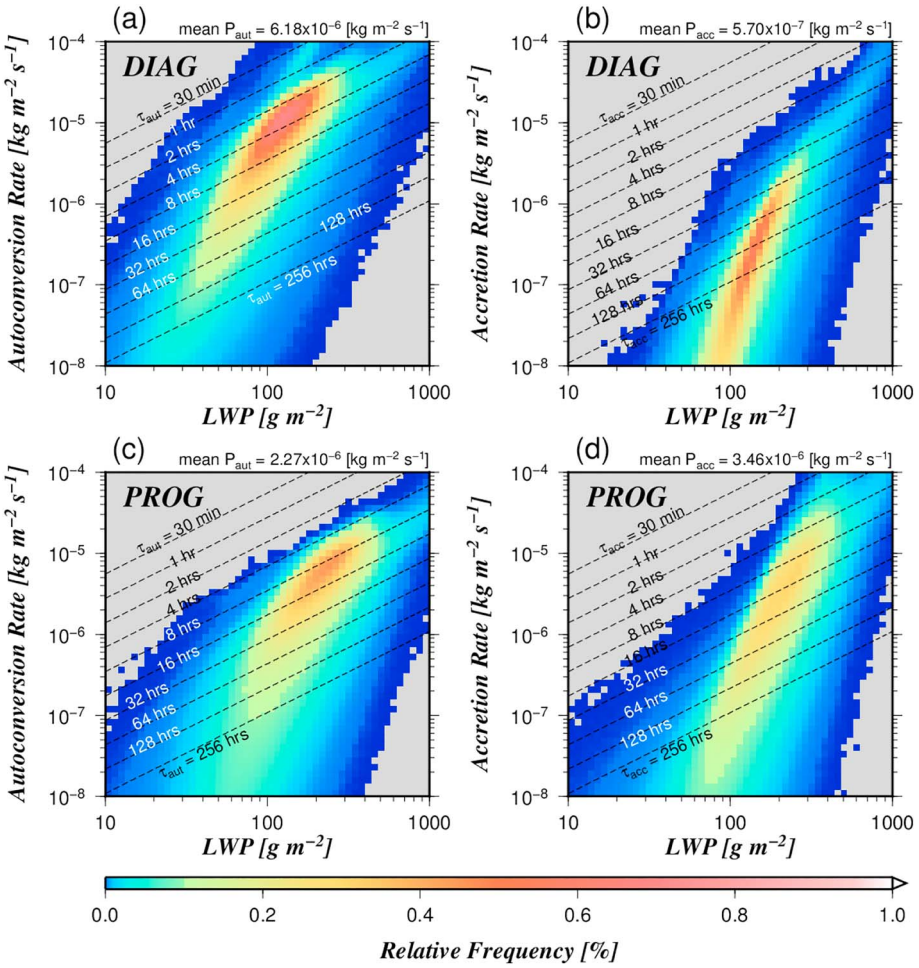

Figure 5. Joint PDF of LWP and vertically integrated process rates for (a, b) diagnostic (DIAG) and (c, d) prognostic (PROG) schemes. The dashed lines indicate the conversion time scale with regard to the autoconversion (τ_{aut}) and accretion (τ_{acc}) processes as references. Global means (60°S to 60°N) of the process rates P_{aut} and P_{acc} are shown at the top right in each panel.

which prolongs the residence time of rainwater. The original MIROC6 implementation with the DIAG scheme still overestimates the precipitation rate, although improvements have been made from the previous version, MIROC5 (Tatebe et al., 2019). Precipitation rate is somewhat decreased (by ~7%) in the PROG scheme (Figure 1g), due to mitigation of radiative cooling in the troposphere. This will be addressed in more detail later (cf. section 3.4).

Consequently, longwave radiative forcing (LWCRF) at the top-of-atmosphere (TOA) is reduced in the PROG scheme (Figure 1h) due to the reduction in cloud ice. The DIAG scheme also underestimates LWCRF, especially over midlatitudes. For shortwave cloud radiative forcing (SWCRF), both DIAG and PROG reflect too brightly over low latitudes (Figure 1i), which implies that cumulus convection is overrepresented in these schemes. These results suggest that in addition to further development of the microphysics framework, improvements in the bulk representation of ice hydrometeors (e.g., Morrison et al., 2015; Milbrandt & Morrison, 2016), as well as in convective parameterization (e.g., Chikira & Sugiyama, 2010; Hirota et al., 2018) are required.

3.2. Warm Rain Microphysics

One of the main differences between the DIAG and PROG schemes lies in the microphysical process rates, summarized in Table 2. Figure 5 illustrates a joint PDF as a function of LWP and vertically integrated process rates. The data presented here are derived from single-layered warm clouds (60°S to 60°N) using 6-hourly instantaneous outputs, so the mean values of vertically integrated process rates, shown at the top right in each panel, differ from the values presented in Table 2.

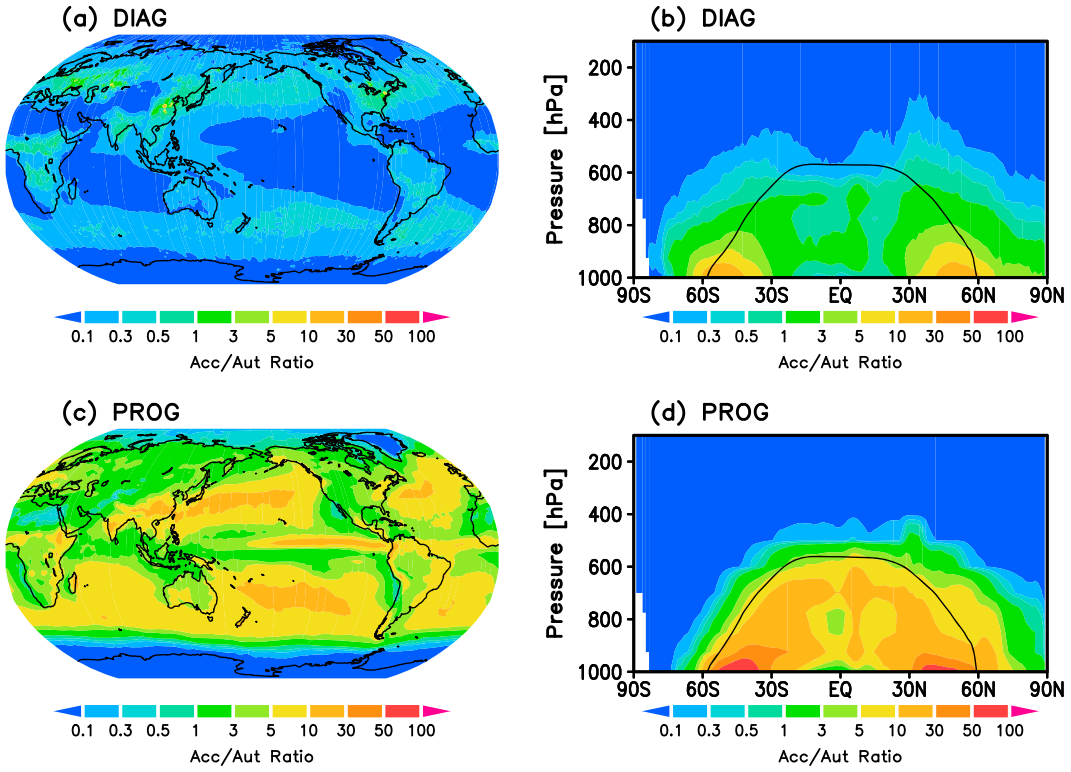

Figure 6. The vertically averaged ratio of accretion to autoconversion (Acc/Aut) for (left) horizontal and (right) vertical distributions obtained from the (top) diagnostic (DIAG) and (bottom) prognostic (PROG) schemes.

In the DIAG scheme, the accretion process is relatively insignificant in our model as all rainwater falls to the surface within a single model time step, such that precipitation occurs primarily by means of the autoconversion process (Figures 5a and 5b). Many of the samples were taken within the autoconversion time scale τ_{aut} range: 8 hr < τ_{aut} < 2 hr (Figure 5a). Use of the alternative autoconversion schemes show a similar relationship between LWP and process rates (Michibata & Takemura, 2015). In contrast, the PROG scheme retains rainwater in the atmosphere across multiple time steps, enhancing the contribution of accretion relative to autoconversion (Figures 5c and 5d). This is consistent with previous studies that tested the prognostic treatment of precipitation (e.g., Gettelman et al., 2015; Posselt & Lohmann, 2008). The dominant autoconversion time scale τ_{aut} ranges from 16 to 4 hr (Figures 5c) and contributes to mitigating the too fast and too frequent light rain issue found in GCMs (Jing et al., 2017; Kay et al., 2018). For LWP > 300 g/m^2, the rain process employed switches to an accretion-dominated regime.

It is important for climate models to characterize the distribution of the Acc/Aut ratio (e.g., Gettelman et al., 2013), because the specific weight of the autoconversion and accretion is related to the susceptibility to aerosols (Feingold et al., 2013; Jiang et al., 2010; Sorooshian et al., 2009), as well as to the precipitation time scale (Suzuki & Stephens, 2009). Figure 6 depicts the horizontal and vertical distribution of the Acc/Aut ratio represented in the model. The DIAG scheme presents a lower Acc/Aut ratio that does not vary very much (<0.1–5.0), whereas the PROG scheme presents larger variability in the Acc/Aut ratio (~0.1–50). This suggests that the PROG scheme is more representative over larger variations in precipitation intensity and time scale. Over continents, a relatively higher Acc/Aut ratio is found for both the DIAG and PROG schemes, due to autoconversion being inhibited in regions where there is higher aerosol concentration. While higher Acc/Aut ratios can only be found over midlatitudes in the DIAG scheme, the PROG scheme presents higher values over the oceanic tropics (i.e., in the eastern Pacific and equatorial Atlantic) where LWP is high. Conversely, the Acc/Aut ratio is lower over the typical stratocumulus deck found over regions such as California, Peru, Namibia, and the Canaries. Lower LWP is characteristic over these regions, and autoconversion is dominant in the formation of precipitation, resulting in a lower Acc/Aut ratio. The vertical structure is also significantly different (Figures 6b and 6d). In PROG, the accretion process is dominant overall (Acc/Aut ratio

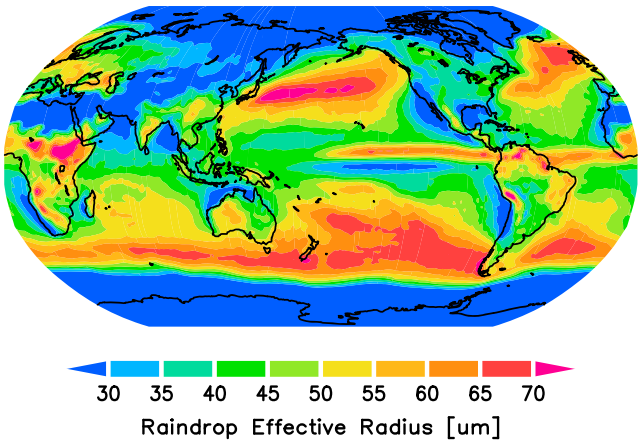

Figure 7. Geographical distribution of the effective raindrop radius below cloud-base simulated by the PROG scheme.

> 10) below the melting layer, and autoconversion is minor except in the upper layer. This microphysical structure is consistent with an observation-based study performed by Wood (2005a).

The balance between autoconversion and accretion is fundamentally related to the representation of raindrop size. This is because autoconversion increases both the mass and number mixing ratios of rain (q_r and N_r) assuming initial raindrops to have a radius of 25 μm, whereas accretion only increases the mass q_r (see also Table 1). Figure 7 depicts the raindrop effective radius as simulated by the PROG scheme. The dominant autoconversion process, especially in the upper portion of clouds, produces numerous small drizzle drops over the calm stratocumulus regions that are characterized by a lower Acc/Aut ratio. Although global observations of raindrop size are limited, MIROC6 PROG successfully captures drizzle droplets (30–50 μm), especially over the marine stratocumulus decks found off the west coasts, where the simulated values agree with several in situ aircraft measurements and field campaigns including: DYCOMS-II (VanZanten et al., 2005), MASE (Wang et al., 2009), ASTEX (Wood, 2005a, 2005b), ARM Azores (Dong et al., 2015; Wu et al., 2015), and VOCALS-REx (Wood et al., 2011; Wang et al., 2012). These results provide evidence that the new PROG scheme is working in a more realistic manner than the previous microphysics scheme, which treated precipitation diagnostically.

It should be noted that the Acc/Aut ratio can be affected by other elements than only the treatment of precipitation. For example, the autoconversion and accretion schemes themselves strongly affect the Acc/Aut ratio, regardless of whether the model adopts a diagnostic or prognostic framework (Hill et al., 2015). This emphasizes the importance of how the model calculates process rates (Michibata & Takemura, 2015) and represents the subgrid-scale variability (Boutle et al., 2014; Lebsock et al., 2013), as well as changing the treatment of precipitation.

3.3. TOA Radiation and Aerosol-Cloud Interactions

To understand how the improvements in microphysics described above affect the radiation and climate fields, we examine the differences between the PD and PI simulations. As a simplification, we employ here the PROG scheme with only liquid rain (snow is the same as DIAG) to isolate the snow radiation effect from the effect that prognostic precipitation has on aerosol-cloud interactions. We evaluate the snow radiative effect further in the next section. The TOA imbalance between longwave and shortwave radiation in the DIAG and PROG schemes is small within the PD environment (−0.31 and −0.21 W/m^2, respectively).

We estimate the effective radiative forcing due to aerosol-cloud interactions (ERF_{aci}), which is defined as the change in net cloud radiative forcing between the PD and PI simulations. The cloud radiative forcing under clean-sky conditions (aerosol free) is used to remove contamination due to aerosol scattering and

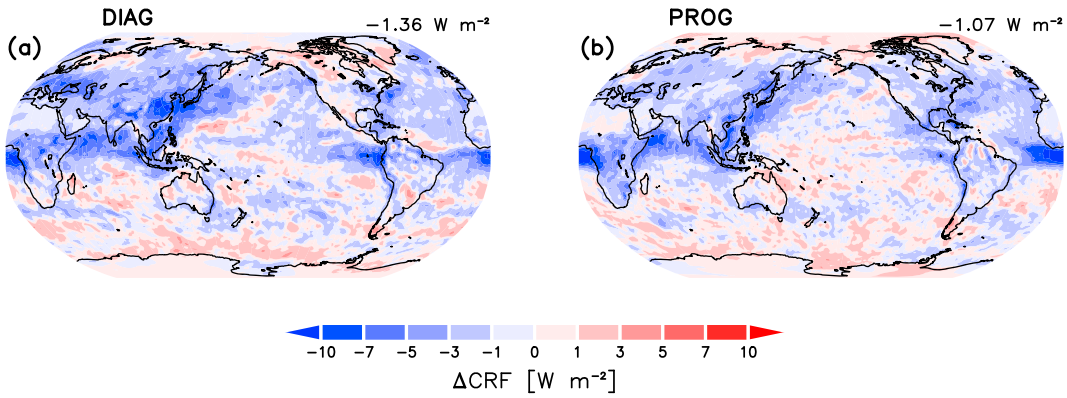

Figure 8. Effective radiative forcing due to aerosol-cloud interactions for the (a) diagnostic (DIAG) and (b) prognostic (PROG) schemes, estimated from changes in cloud radiative forcing (ΔCRF) between the present-day and preindustrial experiments.

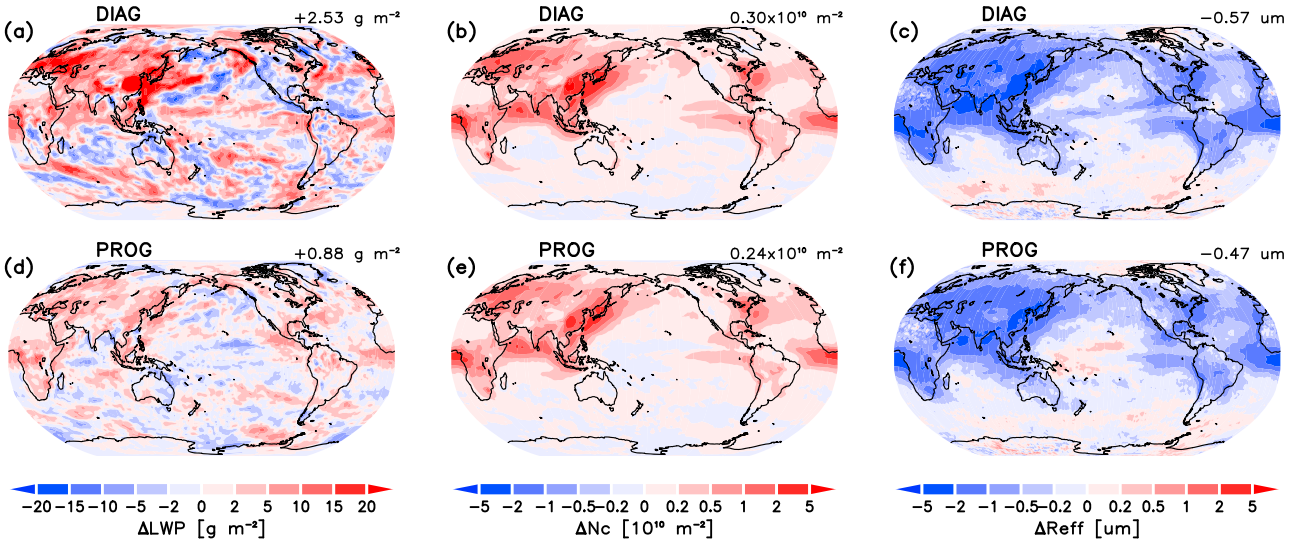

Figure 9. Changes in (a, d) liquid water path (LWP), (b, e) column N_c burden, and (c, f) cloud droplet effective radius R_{eff} from present-day to preindustrial experiments for the (top row) diagnostic (DIAG) and (bottom row) prognostic (PROG) schemes.

absorption following Ghan (2013). Figure 8 illustrates the geographical distribution of the ERF_{aci}. We find strong ERF_{aci} over East Asia, Eurasia, central Africa, the northern Indian Ocean, and the equatorial eastern Pacific. The ERF_{aci} is mitigated, on a near global scale, by switching from the DIAG to PROG scheme, which is consistent with previous findings by Gettelman et al. (2015). Global mean ERF_{aci} is altered from −1.36 W/m^2 (+0.22 W/m^2 for LW and −1.58 W/m^2 for SW) for DIAG to −1.07 W/m^2 (+0.29 W/m^2 for LW and −1.36 W/m^2 for SW) for PROG, mainly due to ΔSWCRF via ΔLWP as shown in Figure 9. Changes in the column N_c burden (ΔN_c) and droplet effective radius (ΔR_{eff}) are less sensitive to change in ERF_{aci}. Cloud cover is also insensitive to the change in the PD–PI anomaly (not shown).

The reduction of the LWP susceptibility to aerosol perturbations in the PROG scheme, from the PI to the PD simulations, is a desirable feature, since most GCMs overestimate the magnitude of the ACI (e.g., Quaas et al., 2009; Wang et al., 2012). Overestimation of the ACI is related to overemphasis in the representation of autoconversion, which suppresses rain generation due to perturbed aerosols, therefore prolonging the cloud lifetime (equation (1)) and resulting in coherent positive LWP susceptibility (Michibata et al., 2016). We conclude that the emphasis given to the accretion process over autoconversion in the PROG scheme (Figures 5 and 6) weakens the LWP susceptibility and thus the magnitude of the ACI.

ERF_{aci} estimated in the PROG scheme is in close agreement with the observational constraints (−1.1 ± 0.4 W/m^2) estimated by Murphy et al. (2009) and with the lower bound of the estimates (−1.0 W/m^2) compiled by Stevens (2015). A recent study suggested that mitigation of the too early rain formation in a GCM can simultaneously overemphasize the anthropogenic aerosol forcing (Jing & Suzuki, 2018). This dichotomy between precipitation and energy (P&E dichotomy) explains why the magnitude of the ACI is highly sensitive to the autoconversion scheme used. It could possibly be eliminated by using a prognostic precipitation scheme, and future work should seek to untangle this self-contradiction (compensating errors) at the fundamental process-level (Gettelman, 2015; Ghan et al., 2016).

As described above, the magnitude of aerosol-cloud interactions is decreased by approximately 21% in the present study, when switching to PROG scheme, which is in agreement with the range of 2–33% reduction suggested by Gettelman et al. (2015). Our results provide a more robust generalization of previously published findings and also emphasize the importance of prognostic precipitation in GCMs for a more realistic representation of aerosol-cloud interactions.

3.4. Snow Radiative Effect

We have so far described aerosol-cloud-radiation interactions, especially for warm-rain processes. Since the previous DIAG scheme in MIROC6 does not calculate the radiative effect of precipitating hydrometeors, we document the effect of the new radiation scheme on model performance. We focus here mainly on the radiative effect of snow, because the radiative impact of rain is negligible (Hill et al., 2018). We have also

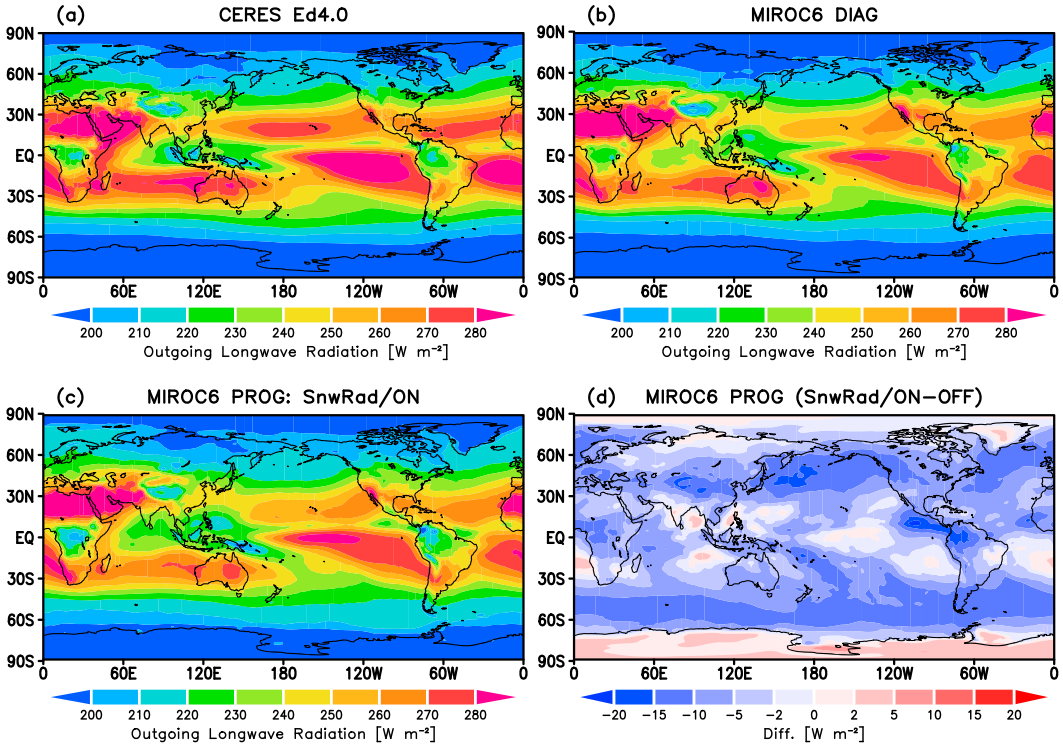

Figure 10. Global annual mean outgoing longwave radiation for (a) CERES observations, (b) MIROC6 DIAG, (c) MIROC6 PROG, and (d) the difference between the PROG scheme without the snow radiative effect and the standard configuration (ON/SnwRad − OFF/SnwRad).

estimated rain radiative effect by conducting sets of simulations with and without radiative effect of rainwater (not shown) to find that the global mean difference in NetCRF between the two experiments was negligibly small (−0.09 W/m^2).

Sets of simulations were performed using the PROG scheme both with and without the snow radiation effect, as summarized in Table 2. Although there has been some similar research recently (e.g., Chen et al., 2018; Li et al., 2016), our findings related to the impact of the snow radiative effect on model performance are expected to make a valuable contribution because most GCMs still ignore the radiative effect of snow.

Figure 10 illustrates outgoing longwave radiation (OLR) and shows that both the DIAG and PROG schemes are in good agreement with the CERES satellite observations. The difference between PROG ON/SnwRad and OFF/SnwRad yields an almost global negative anomaly in OLR (Figure 10d). This is because the suspended snowflakes trap terrestrial radiation. The negative anomaly is relatively large over midlatitudes where SWP is large, and the geographical pattern is similar to that found by Li et al. (2014). The accumulated precipitating ice hydrometeors reflect solar radiation simultaneously, but the radiative effect is more sensitive at longwave. The differences in global mean OLR and OSR between the ON/SnwRad and OFF/SnwRad experiments are significant, 6.4 and 5.1 W/m^2 in absolute values, respectively (i.e., $\Delta F_{\mathrm{net}} = 1.3$ W/m^2). These values are larger than those previously estimated by Li et al. (2014) and Chen et al. (2018), because MIROC6 PROG has more SWP than the models used in previous studies. Given that the real atmosphere has more TIWP compared to that in models (Figure 1c), the radiative impacts should be more significant.

Incorporating the snow radiation effect into the model leads to stabilization of the troposphere. Net radiative cooling, the imbalance between shortwave heating and longwave cooling, is weaker in PROG ON/SnwRad (104.3 W/m^2) than in PROG OFF/SnwRad (108.1 W/m^2), and closely agrees in both with regard to the corresponding summation of sensible and latent heats, 104.1and 107.9 W/m^2, respectively. These values are consistent with the observational constraints on the energy budget (~106–108 W/m^2) described by L'Ecuyer et al. (2015) and Stephens and L'Ecuyer (2015).

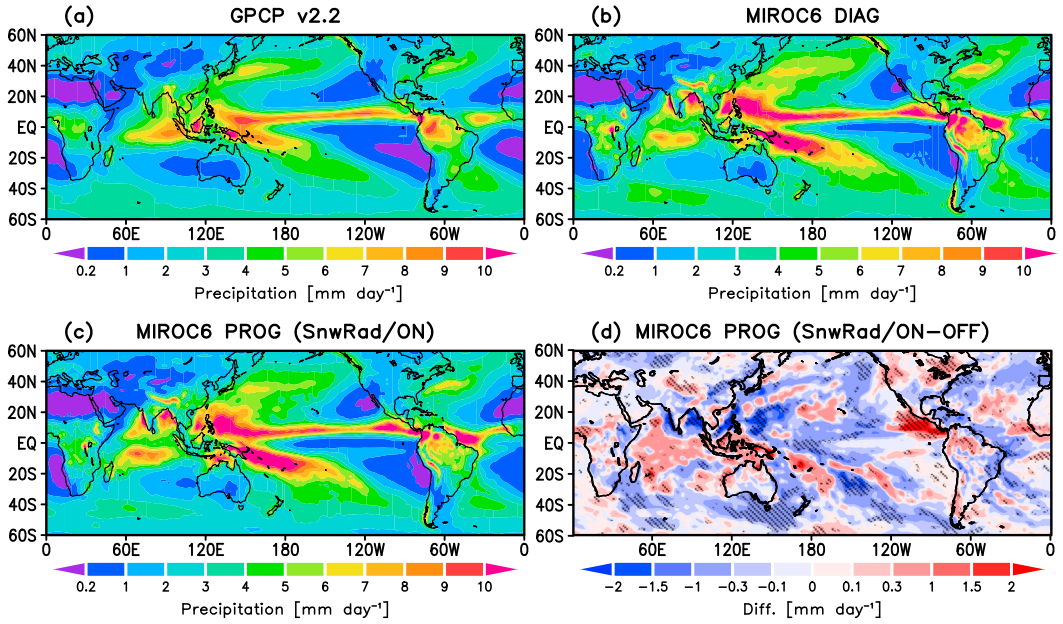

Figure 11. Global annual mean precipitation rate for (a) GPCP observations, (b) MIROC6 DIAG, (c) MIROC6 PROG, and (d) the difference between the PROG scheme without snow radiative effect and the standard configuration (ON/SnwRad − OFF/SnwRad). The regions where the difference between ON/SnwRad and OFF/SnwRad is significant (larger than 2 standard deviations of the interannual variability) are hatched. GPCP = Global Precipitation Climatology Project; PROG = prognostic.

Figure 11 shows the precipitation rate for GPCP observations, MIROC6 simulations for DIAG and PROG, and the resulting changes between the ON/SnwRad and OFF/SnwRad. Both the DIAG and PROG schemes are representative of the qualitative distribution of precipitation, yet MIROC6 somewhat quantitatively overestimates the precipitation rate, as discussed in Tatebe et al. (2019). Nevertheless, PROG reduces the overestimation of precipitation in comparison to the DIAG scheme (Figures 11b and 11c), especially over the north Pacific, off the west coast of Australia, over Peru, and Namibia, and over the Amazon.

On the other hand, the large model bias in relation to the GPCP observations is still evident in the PROG scheme, especially over the tropics, where convective activity is strong (e.g., in the Arabian Sea and Bay of Bengal, the Philippines, and the Intertropical Convergence Zone/South Pacific Convergence Zone), due to the moist free troposphere that triggers convection (Hirota et al., 2018). Note that the large precipitation bias worsens if the model does not incorporate the radiative effect of snow (Figure 11d) over these regions. It can be assumed that the stronger radiative cooling derived in the OFF/SnwRad leads to vertical destabilization and thus heavier precipitation. In fact, the net effect of the TOA imbalance (ΔF_{net}) and the difference in radiative cooling (i.e., $-1.3 + 108.1 - 104.3 = \sim 2.5$ W/m^2) is balanced with the simulated difference in precipitation rate between the ON/SnwRad and OFF/SnwRad (i.e., 0.095 mm/day $= \sim 2.7$ W/m^2).

As we described earlier, the model prognosed only the large-scale contribution of precipitating hydrometeors. However, these results suggest that the prognostic precipitation, including its radiative effect, can alter the precipitation rate as well as its global distribution, by modifying the vertical circulation (not shown) via cloud-radiation-dynamics interactions (e.g., Li et al., 2014) due to the mitigation of radiative cooling in the atmosphere. Many GCMs, in addition to MIROC6, tend to overestimate global mean precipitation (e.g., Guo et al., 2014; Salzmann et al., 2010; Stephens et al., 2012; Sud et al., 2013; Sant et al., 2015; Wang et al., 2011). The mitigation of the radiative cooling due to snow will contribute to reducing the common bias in CMIP models. If observed solid hydrometeors in the atmosphere are larger than those in the model simulations, the radiative cooling will be more moderated. The modeled climate sensitivity will also be modified (e.g., Bony et al., 2015; Sherwood et al., 2014). The results detailed above strongly support the importance of incorporating the snow radiative effect in GCMs to achieve more reliable climate research outputs. The application within models of prognostic precipitation for both liquid and solid species, as well as their radiative calculation, will contribute to advances in global climate modeling.

4. Summary and Future Work

We have developed a two-moment microphysics scheme with prognostic precipitation for both rain and snow and incorporated it into an aerosol-climate model, the MIROC6-SPRINTARS GCM. The radiative transfer calculation for precipitation has also been coupled to the new scheme. To explore the impact of applying this treatment for precipitation and its radiative effect on the climate simulation, we evaluated the performance of the traditional DIAG scheme and the newly introduced PROG scheme, with and without inclusion of the snow radiative effect, using multisatellite data sets. Although not all changes are attributed to the different treatments of precipitation, we have obtained significant improvements by applying prognostic precipitation framework in our model described below.

The new PROG scheme reproduced well the observed statistics in terms of cloud microphysics and macrophysics, as well as the TOA radiation. The ratio of accretion to autoconversion (Acc/Aut) was significantly increased in the PROG simulation, which was in closer agreement with the observed trend based on in situ measurements (Gettelman et al., 2013). This characteristic of the PROG scheme is consistent with previous studies of the application of prognostic precipitation in GCMs (e.g., Gettelman et al., 2015; Posselt & Lohmann, 2008), in that the rainwater can reside in the atmosphere across multiple time steps. Use of prognostic precipitation slowed down the autoconversion time scale, mitigating the premature onset of rain, which is regarded as a common issue in GCMs (Jing et al., 2017). The PROG scheme successfully modeled smaller raindrops (drizzle), which are frequently observed off the west coast of California, and over Peru, the Canaries and Namibia, as a result of improved parameterization of the relative weight of autoconversion (characterized by increases in both q_r and N_r) and accretion (with an increase only in q_r).

The treatment of precipitation in the model also significantly altered the vertical structure of hydrometeors. Although the global mean CLWP decreased in PROG, because some cloud water shifted to the rain class, q_c increased for lower altitudes (>800 hPa), which resulted in an increase of ~38% in the occurrence frequency of single-layered warm clouds. The overemphasized supercooled liquid fraction in the DIAG scheme was reduced in the PROG scheme due to depletion of cloud liquid water from coexisting ice hydrometeors via the BF process. As a result, TIWP (i.e., CIWP + SWP) was increased significantly by switching from the DIAG to PROG framework, providing comparable results to the CloudSat and CALIPSO retrievals. The changes in vertical distribution of hydrometeors and thus the phase partitioning of liquid and ice can further alter the modeled climate sensitivity (Tan et al., 2016). This is an area that would benefit from further investigation.

We have quantified the anthropogenic aerosol forcing by looking at the differences in TOA radiation between PD and PI. The PROG scheme reduced the magnitude of ERF_{aci} by approximately 21%, which lies within the range of the 2–33% reduction suggested by Gettelman et al. (2015). The reduction of ERF_{aci} in PROG was fundamentally related to the mitigation of LWP susceptibility to perturbed aerosols from the PI to the PD simulations. The autoconversion process provides the only pathway through which aerosols can influence rain formation (see equation (1)) and therefore the LWP susceptibility (Michibata et al., 2016). It can therefore be inferred that improvements in microphysical process rates are concurrent with improvement in ERF_{aci}.

To evaluate the snow radiative effect in the new PROG scheme, sets of simulations with and without the snow radiative effect (ON/SnwRad and OFF/SnwRad) were performed. Precipitating ice affected both longwave and shortwave radiation significantly, with the former found to be more sensitive (changes in OLR and OSR were 6.4 and 5.1 W/m^2 in absolute values, respectively). Simulation with the ON/SnwRad reduced the precipitation rate by ~0.1 mm/day compared to the OFF/SnwRad, due to moderation of radiative cooling that stabilizes the troposphere. In our model, the particle shapes of solid hydrometeors are prescribed (hexagonal columns for cloud ice; dendrite crystals for snow). It is recommended that a further study is conducted into particle species and shape sensitivity. In addition, arbitrary unphysical parameter, such as the ice-to-snow autoconversion threshold size, should be avoided in a further model development. Taking this into account, incorporation of a single ice parameterization (Morrison & Milbrandt, 2015) into GCMs could be one of the solutions for better describing ice morphology while ensuring continuity of ice growth (Dietlicher et al., 2018; Eidhammer et al., 2017; Zhao et al., 2017).

Our study has shown that application of prognostic precipitation for both liquid and solid hydrometeors, as well as for their radiative calculation, will lead to promising advances in global climate modeling. If we do not

include prognostic precipitation in GCMs, our confidence in simulating aerosol-cloud-precipitation-climate interactions will remain low.

Acknowledgments
The authors would like to thank the developers of both SPRINTARS and MIROC. Codes of the new microphysics and radiation scheme were optimized by Koji Ogochi. Simulations by MIROC-SPRINTARS were executed with the SX-ACE supercomputer system of the National Institute for Environmental Studies, Japan. MODIS Collection 6, Level 3 products are available through the LAADS website (https://ladsweb.modaps.eosdis.nasa.gov/). SSMIS instrument data are obtained from the Remote Sensing Systems data services website (http://www.remss.com/missions/ssmi). ISCCP D2 data sets are also available online (http://isccp.giss.nasa.gov/products/browsed2.html). GPCP version 2.2 can be obtained from NASA Goddard Space Flight Center (http://precip.gsfc.nasa.gov). CERES EBAF-TOA Edition 4.0 products are available from the NASA Langley Research Center (http://ceres.larc.nasa.gov/order_data.php). The CloudSat data products were provided by the CloudSat Data Processing Center at CIRA/Colorado State University (http://www.cloudsat.cira.colostate.edu). CALIPSO-GOCCP data set version 3.1.2 was obtained from ClimServ data center (http://climserv.ipsl.polytechnique.fr/cfmip-obs/Calipso_goccp.html). This study was supported by the JSPS KAKENHI Grant-in-Aid for Research Fellows (JP15J05544, JP18J00301, and JP15H01728); the Integrated Research Program for Advancing Climate Models (TOUGOU program) from the Ministry of Education, Culture, Sports, Science and Technology (MEXT), Japan; the Environment Research and Technology Development Fund (S-12-3) of the Environmental Restoration and Conservation Agency, Japan; and the Collaborative Research Program of Research Institute for Applied Mechanics, Kyushu University. K. Suzuki was supported by NOAA's Climate Program Office's Modeling, Analysis, Predictions, and Projections program with grant NA15OAR4310153. The MIROC6-SPRINTARS simulation data used for analysis are available at https://doi.org/10.5281/zenodo.2584312 website. The authors are grateful to Ian Boutle (UK Met Office) and one anonymous reviewer for providing constructive suggestions and comments, that helped to improve the manuscript.

References

Abdul-Razzak, H., & Ghan, J. (2000). A parameterization of aerosol activation 2. Multiple aerosol types. *Journal of Geophysical Research*, *105*, 6837–6844.

Adler, R. F., Huffman, G. J., Chang, A., Ferraro, R., Xie, P.-P., Janowiak, J., et al. (2003). The Version-2 Global Precipitation Climatology Project (GPCP) monthly precipitation analysis (1979–present). *Journal of Hydrometeorology*, *4*, 1147–1167.

Albrecht, B. A. (1989). Aerosols, cloud microphysics, and fractional cloudiness. *Science*, *245*, 1227–1230.

Barthazy, E., & Schefold, R. (2006). Fall velocity of snowflakes of different riming degree and crystal types. *Atmospheric Research*, *82*, 391–398.

Beheng, K. D. (1994). A parameterization of warm cloud microphysical conversion processes. *Atmospheric Research*, *33*, 193–206.

Bender, F. A.-M., Frey, L., McCoy, D. T., Grosvenor, D. P., & Mohrmann, J. K. (2018). Assessment of aerosol–cloud–radiation correlations in satellite observations, climate models and reanalysis. *Climate Dynamics*. https://doi.org/10.1007/s00382-018-4384-z

Bergeron, T. (1935). On the physics of cloud and precipitation. Proces verbaux de l'association de meteorologie, intl. union of geod. and geophys., paris (pp. 156–178).

Berry, E. X. (1968). Modification of the Warm Rain Process. In *Proceedings first conf. on weather modification Albany, NY. American Meteorological Society paper presented at 1st National Conference on Weather Modification, April 28–May 1*, pp. 81–85.

Bodas-Salcedo, A., Webb, M. J., Bony, S., Chepfer, H., Dufresne, J.-L., Klein, S. A., et al. (2011). COSP: Satellite simulation software for model assessment. *Bulletin of the American Meteorological Society*, *92*, 1023–1043.

Bony, S., Stevens, B., Frierson, D. M. W., Jakob, C., Kageyama, M., Pincus, R., et al. (2015). Clouds, circulation and climate sensitivity. *Nature Geoscience*, *8*, 261–268.

Boutle, I. A., Abel, S. J., Hill, P. G., & Morcrette, C. J. (2014). Spatial variability of liquid cloud and rain: Observations and microphysical effects. *Quarterly Journal of the Royal Meteorological Society*, *140*, 583–594.

Calisto, M., Folini, D., Wild, M., & Bengtsson, L. (2014). Cloud radiative forcing intercomparison between fully coupled CMIP5 models and CERES satellite data. *Annales Geophysicae*, *32*, 793–807.

Chen, Y. W., Seiki, T., Kodama, C., Satoh, M., & Noda, A. T. (2018). Impact of precipitating ice hydrometeors on longwave radiative effect estimated by a global cloud-system resolving model. *Journal of Advances in Modeling Earth Systems*, *10*, 284–296. https://doi.org/10.1002/2017MS001180

Chepfer, H., Bony, S., Winker, D., Cesana, G., Dufresne, J. L., Minnis, P., et al. (2010). The GCM-oriented CALIPSO cloud product (CALIPSO-GOCCP). *Journal of Geophysical Research*, *115*, D00H16. https://doi.org/10.1029/2009JD012251

Chikira, M., & Sugiyama, M. (2010). A cumulus parameterization with state-dependent entrainment rate. Part I: Description and sensitivity to temperature and humidity profiles. *Journal of the Atmospheric Sciences*, *67*, 2171–2193.

Chosson, F., Vaillancourt, P. A., Milbrandt, J. A., Yau, M. K., & Zadra, A. (2014). Adapting two-moment microphysics schemes across model resolutions: Subgrid cloud and precipitation fraction and microphysical sub-time step. *Journal of the Atmospheric Sciences*, *71*, 2635–2653.

Cotton, W. R., Tripolo, G. J., Rauber, R. M., & Mulvihill, E. A. (1986). Numerical simulation of the effects of varying ice crystal nucleation rates and aggregation processes on orographic snowfall. *Journal of Climate and Applied Meteorology*, *25*, 1658–1680.

Dietlicher, R., Neubauer, D., Lohmann, U., & Science, C. (2018). Prognostic parameterization of cloud ice with a single category in the aerosol-climate model ECHAM (v6.3.0)-HAM (v2.3). *Geoscientific Model Development*, *11*, 1557–1576.

Dong, X., Schwantes, A. C., Xi, B., & Wu, P. (2015). Investigation of the marine boundary layer cloud and CCN properties under coupled and decoupled conditions over the Azores. *Journal of Geophysical Research: Atmospheres*, *120*, 6179–6191. https://doi.org/10.1002/2014JD022939

Eidhammer, T., Morrison, H., Mitchell, D., Gettelman, A., & Erfani, E. (2017). Improvements in global climate model microphysics using a consistent representation of ice particle properties. *Journal of Climate*, *30*, 609–629.

Fan, J., Ghan, S., Ovchinnikov, M., Liu, X., Rasch, P. J., & Korolev, A. (2011). Representation of Arctic mixed-phase clouds and the Wegener-Bergeron- Findeisen process in climate models: Perspectives from a cloud-resolving study. *Journal of Geophysical Research*, *116*, D00T07. https://doi.org/10.1029/2010JD015375

Feingold, G., McComiskey, A., Rosenfeld, D., & Sorooshian, A. (2013). On the relationship between cloud contact time and precipitation susceptibility to aerosol. *Journal of Geophysical Research: Atmospheres*, *118*, 10,544–10,554. https://doi.org/10.1002/jgrd.50819

Findeisen, Z. (1938). Kolloid meteorologische vorgange bei neiderschlags-bildung. *Meteorologische Zeitschrift*, *55*, 121–133.

Gettelman, A. (2015). Putting the clouds back in aerosol–cloud interactions. *Atmospheric Chemistry and Physics*, *15*(21), 12397–12411.

Gettelman, A., & Morrison, H. (2015). Advanced two-moment bulk microphysics for global models. Part I: Off-line tests and comparison with other schemes. *Journal of Climate*, *28*, 1268–1287.

Gettelman, A., Morrison, H., Santos, S., Bogenschutz, P., & Caldwell, P. M. (2015). Advanced two-moment bulk microphysics for global models. Part II: Global model solutions and aerosol–cloud interactions. *Journal of Climate*, *28*, 1288–1307.

Gettelman, A., Morrison, H., Terai, C. R., & Wood, R. (2013). Microphysical process rates and global aerosol–cloud interactions. *Atmospheric Chemistry and Physics*, *13*, 9855–9867.

Gettelman, A., & Sherwood, S. C. (2016). Processes responsible for cloud feedback. *Current Climate Change Reports*, *2*, 179–189.

Ghan, S. J. (2013). Technical note: Estimating aerosol effects on cloud radiative forcing. *Atmospheric Chemistry and Physics*, *13*, 9971–9974.

Ghan, S. J., & Easter, R. C. (1992). Computationally efficient approximations to stratiform cloud microphysics parameterization. *Monthly Weather Review*, *120*, 1572–1582.

Ghan, S., Wang, M., Zhang, S., Ferrachat, S., Gettelman, A., Griesfeller, J., et al. (2016). Challenges in constraining anthropogenic aerosol effects on cloud radiative forcing using present-day spatiotemporal variability. *Proceedings of the National Academy of Sciences*, *113*, 5804–5811.

Golaz, J.-C., Horowitz, L. W., & Levy, H. (2013). Cloud tuning in a coupled climate model: Impact on 20th century warming. *Geophysical Research Letters*, *40*, 2246–2251. https://doi.org/10.1002/grl.50232

Guo, H., Golaz, J.-C., Donner, L. J., Ginoux, P., & Hemler, R. S. (2014). Multivariate probability density functions with dynamics in the GFDL atmospheric general circulation model: Global tests. *Journal of Climate*, *27*, 2087–2108.

Hill, P. G., Chiu, J. C., Allan, R., & Chern, J. D. (2018). Characterizing the radiative effect of rain using a global ensemble of cloud resolving simulations. *Journal of Advances in Modeling Earth Systems*, *10*, 2453–2470. https://doi.org/10.1029/2018MS001415

Hill, A. A., Shipway, B. J., & Boutle, I. A. (2015). How sensitive are aerosol-precipitation interactions to the warm rain representation? *Journal of Advances in Modeling Earth Systems*, *7*, 987–1004. https://doi.org/10.1002/2014MS000422

Hirota, N., Ogura, T., Tatebe, H., Shiogama, H., Kimoto, M., & Watanabe, M. (2018). Roles of shallow convective moistening in the eastward propagation of the MJO in MIROC6. *Journal of Climate*, *31*, 3033–3047.

Janssens-Maenhout, G., Dentener, F., van Aardenne, J., Monni, S., Pagliari, V., Orlandini, L., et al. (2012). EDGAR-HTAP: A harmonized gridded air pollution emission dataset based on national inventories.

Jiang, H., Feingold, G., & Sorooshian, A. (2010). Effect of aerosol on the susceptibility and efficiency of precipitation in warm trade cumulus clouds. *Journal of the Atmospheric Sciences*, *67*, 3525–3540.

Jing, X., & Suzuki, K. (2018). The impact of process-based warm rain constraints on the aerosol indirect effect. *Geophysical Research Letters*, *45*, 10,729–10,737.

Jing, X., Suzuki, K., Guo, H., Goto, D., Ogura, T., Koshiro, T., & Mülmenstädt, J. (2017). A multimodel study on warm precipitation biases in global models compared to satellite observations. *Journal of Geophysical Research: Atmospheres*, *122*, 11,806–11,824. https://doi.org/10.1002/2017JD027310

Juang, H.-M. H., & Hong, S.-Y. (2010). Forward semi-Lagrangian advection with mass conservation and positive definiteness for falling hydrometeors. *Monthly Weather Review*, *138*, 1778–1791.

Kato, T. (1995). A box-Lagrangian Rain-Drop Scheme. *Journal of the Meteorological Society of Japan*, *73*, 241–245.

Kay, J. E., L'Ecuyer, T., Pendergrass, A., Chepfer, H., Guzman, R., & Yettella, V. (2018). Scale-aware and definition-aware evaluation of modeled near-surface precipitation frequency using CloudSat observations. *Journal of Geophysical Research: Atmospheres*, *123*, 4294–4309. https://doi.org/10.1002/2017JD028213

Khairoutdinov, M., & Kogan, Y. (2000). A new cloud physics parameterization in a large-eddy simulation model of marine stratocumulus. *Monthly Weather Review*, *128*, 229–243.

King, N. J., Bower, K. N., Crosier, J., & Crawford, I. (2013). Evaluating MODIS cloud retrievals with in situ observations from VOCALS-REx. *Atmospheric Chemistry and Physics*, *13*, 191–209.

Klein, S. A., & Hartmann, D. L. (1993). The seasonal cycle of low stratiform clouds. *Journal of Climate*, *6*, 1587–1606.

Komurcu, M., Storelvmo, T., Tan, I., Lohmann, U., Yun, Y., Penner, J. E., et al. (2014). Intercomparison of the cloud water phase among global climate models. *Journal of Geophysical Research: Atmospheres*, *119*, 3372–3400. https://doi.org/10.1002/2013JD021119

L'Ecuyer, T. S., Beaudoing, H. K., Rodell, M., Olson, W., Lin, B., Kato, S., et al. (2015). The observed state of the energy budget in the early 21st century. *Journal of Climate*, *28*, 8319–8346.

Lebsock, M. D., L'Ecuyer, T. S., & Stephens, G. L. (2011). Detecting the ratio of rain and cloud water in low-latitude shallow marine clouds. *Journal of Applied Meteorology and Climatology*, *50*, 419–432. https://doi.org/10.1175/2010JAMC2494.1

Lebsock, M., Morrison, H., & Gettelman, A. (2013). Microphysical implications of cloud-precipitation covariance derived from satellite remote sensing. *Journal of Geophysical Research: Atmospheres*, *118*, 6521–6533. https://doi.org/10.1002/jgrd.50347

Li, J.-L. F., Forbes, R. M., Waliser, D. E., Stephens, G., & Lee, S. (2014). Characterizing the radiative impacts of precipitating snow in the ECMWF integrated forecast system global model. *Journal of Geophysical Research: Atmospheres*, *119*, 9626–9637. https://doi.org/10.1002/2014JD021450

Li, J.-L. F., Lee, W.-L., Waliser, D. E., Neelin, J. D., Stachnik, J. P., & Lee, T. (2014). Cloud-precipitation-radiation-dynamics interaction in global climate models: A snow and radiation interaction sensitivity experiment. *Journal of Geophysical Research: Atmospheres*, *119*, 3809–3824. https://doi.org/10.1002/2013JD021038

Li, J.-L. F., Lee, W.-L., Yu, J.-Y., Hulley, G., Fetzer, E., Chen, Y.-C., & Wang, Y.-H. (2016). The impacts of precipitating hydrometeors radiative effects on land surface temperature in contemporary GCMs using satellite observations. *Journal of Geophysical Research: Atmospheres*, *121*, 67–79. https://doi.org/10.1002/2015JD023776

Li, J. L. F., Waliser, D. E., Chen, W. T., Guan, B., Kubar, T., Stephens, G., et al. (2012). An observationally based evaluation of cloud ice water in CMIP3 and CMIP5 GCMs and contemporary reanalyses using contemporary satellite data. *Journal of Geophysical Research*, *117*, D16105. https://doi.org/10.1029/2012JD017640

Liu, Y., & Daum, P. H. (2004). Parameterization of the autoconversion process. Part I: Analytical formulation of the Kessler-type parameterizations. *Journal of the Atmospheric Sciences*, *61*, 1539–1548.

Loeb, N. G., Doelling, D. R., Wang, H., Su, W., Nguyen, C., Corbett, J. G., et al. (2018). Surface irradiances of edition 4.0 Clouds and the Earth's Radiant Energy System (CERES) Energy Balanced and Filled (EBAF) data product. *Journal of Climate*, *31*, 4501–4527.

Marchand, R., Mace, G. G., Ackerman, T., & Stephens, G. (2008). Hydrometeor detection using Cloudsat—An earth-orbiting 94-GHz cloud radar. *Journal of Atmospheric and Oceanic Technology*, *25*, 519–533.

Matus, A. V., & L'Ecuyer, T. S. (2017). The role of cloud phase in Earth's radiation budget. *Journal of Geophysical Research: Atmospheres*, *122*, 2559–2578. https://doi.org/10.1002/2016JD025951

McCoy, D. T., Tan, I., Hartmann, D. L., Zelinka, M. D., & Storelvmo, T. (2016). On the relationships among cloud cover, mixed-phase partitioning, and planetary albedo in GCMs. *Journal of Advances in Modeling Earth Systems*, *8*, 650–668. https://doi.org/10.1002/2015MS000589

Merk, D., Deneke, H., Pospichal, B., & Seifert, P. (2016). Investigation of the adiabatic assumption for estimating cloud micro- and macrophysical properties from satellite and ground observations. *Atmospheric Chemistry and Physics*, *16*, 933–952.

Michibata, T., Kawamoto, K., & Takemura, T. (2014). The effects of aerosols on water cloud microphysics and macrophysics based on satellite-retrieved data over East Asia and the North Pacific. *Atmospheric Chemistry and Physics*, *14*, 11935–11948.

Michibata, T., Suzuki, K., Sato, Y., & Takemura, T. (2016). The source of discrepancies in aerosol–cloud–precipitation interactions between GCM and A-Train retrievals. *Atmospheric Chemistry and Physics*, *16*, 15413–15424.

Michibata, T., & Takemura, T. (2015). Evaluation of autoconversion schemes in a single model framework with satellite observations. *Journal of Geophysical Research: Atmospheres*, *120*, 9570–9590. https://doi.org/10.1002/2015JD023818

Milbrandt, J. A., & Morrison, H. (2016). Parameterization of cloud microphysics based on the prediction of bulk ice particle properties. Part III: Introduction of multiple free categories. *Journal of the Atmospheric Sciences*, *73*, 975–995.

Morrison, H., & Gettelman, A. (2008). A new two-moment bulk stratiform cloud microphysics scheme in the Community Atmosphere Model, version 3 (CAM3). Part I: Description and numerical tests. *Journal of Climate*, *21*, 3642–3659.

Morrison, H., & Milbrandt, J. A. (2015). Parameterization of cloud microphysics based on the prediction of bulk ice particle properties. Part I: Scheme description and idealized tests. *Journal of the Atmospheric Sciences*, *72*, 287–311.

Morrison, H., Milbrandt, J. A., Bryan, G. H., Ikeda, K., Tessendorf, S. A., & Thompson, G. (2015). Parameterization of cloud microphysics based on the prediction of bulk ice particle properties. Part II: Case study comparisons with observations and other schemes. *Journal of the Atmospheric Sciences*, *72*, 312–339.

Mulcahy, J. P., Jones, C., Sellar, A., Johnson, B., Boutle, I. A., Jones, A., et al. (2018). Improved aerosol processes and effective radiative forcing in HadGEM3 and UKESM1. *Journal of Advances in Modeling Earth Systems*, *10*, 2786–2805. https://doi.org/10.1029/2018MS001464

Murphy, D. M., Solomon, S., Portmann, R. W., Rosenlof, K. H., Forster, P. M., & Wong, T. (2009). An observationally based energy balance for the Earth since 1950. *Journal of Geophysical Research*, *114*, D17107. https://doi.org/10.1029/2009JD012105

Nakajima, T. Y., Suzuki, K., & Stephens, G. L. (2010a). Droplet growth in warm water clouds observed by the A-Train. Part II: A multisensor view. *Journal of the Atmospheric Sciences*, *67*, 1897–1907.

Nakajima, T. Y., Suzuki, K., & Stephens, G. L. (2010b). Droplet growth in warm water clouds observed by the A-Train. Part I: Sensitivity analysis of the MODIS-derived cloud droplet sizes. *Journal of the Atmospheric Sciences*, *67*, 1884–1896.

Nam, C., Bony, S., Dufresne, J.-L., & Chepfer, H. (2012). The 'too few, too bright' tropical low-cloud problem in CMIP5 models. *Geophysical Research Letters*, *39*, L21801. https://doi.org/10.1029/2012GL053421

Park, S., & Bretherton, C. S. (2009). The University of Washington shallow convection and moist turbulence schemes and their impact on climate simulations with the community atmosphere model. *Journal of Climate*, *22*, 3449–3469.

Partain, P. (2007). Cloudsat ECMWF-AUX auxiliary data process description and interface control document. Cooperative Institute for Research in the Atmosphere, Colorado State University pp. 10.

Passarelli, R. E. (1978). An approximate analytical model of the vapor deposition and aggregation growth of snowflakes. *Journal of the Atmospheric Sciences*, *35*, 118–124.

Platnick, S. (2000). Vertical photon transport in cloud remote sensing problems. *Journal of Geophysical Research*, *105*, 22919–22935.

Platnick, S., Meyer, K. G., King, M. D., Wind, G., Amarasinghe, N., Marchant, B., et al. (2017). The MODIS cloud optical and microphysical products: Collection 6 updates and examples from Terra and Aqua. *IEEE Transactions on Geoscience and Remote Sensing*, *55*, 502–525.

Posselt, R., & Lohmann, U. (2008). Introduction of prognostic rain in ECHAM5: Design and single column model simulations. *Atmospheric Chemistry and Physics*, *8*, 2949–2963.

Posselt, R., & Lohmann, U. (2009). Sensitivity of the total anthropogenic aerosol effect to the treatment of rain in a global climate model. *Geophysical Research Letters*, *36*, L02805. https://doi.org/10.1029/2008GL035796

Quaas, J., Ming, Y., Menon, S., Takemura, T., Wang, M., Penner, J. E., et al. (2009). Aerosol indirect effects—General circulation model intercomparison and evaluation with satellite data. *Atmospheric Chemistry and Physics*, *9*, 8697–8717.

Randerson, J. T., van der Werf, G. R., Giglio, L., Collatz, G. J., & Kasibhatla, P. S. (2013). Global fire emissions database, version 3.1. ORNL DAAC, Oak Ridge, Tennessee.

Reisner, J., Rasmussen, R. M., & Bruintjes, R. T. (1998). Explicit forecasting of supercooled liquid water in winter storms using the MM5 mesoscale model. *Quarterly Journal of the Royal Meteorological Society*, *124*, 1071–1107.

Reitter, S., Fröhlich, K., Seifert, A., Crewell, S., & Mech, M. (2011). Evaluation of ice and snow content in the global numerical weather prediction model GME with CloudSat. *Geoscientific Model Development*, *4*, 579–589.

Rogers, R. R., Baumgardner, D., Ethier, S. A., Carter, D. A., & Ecklund, W. L. (1993). Comparison of raindrop size distributions measured by radar wind profiler and by airplane. *Journal of Applied Meteorology*, *32*, 694–699.

Rossow, W. B., & Schiffer, R. A. (1999). Advances in understanding clouds from ISCCP. *Bulletin of the American Meteorological Society*, *80*, 2261–2287.

Rotstayn, L. D. (1997). A physically based scheme for the treatment of stratiform clouds and precipitation in large-scale models. I: Description and evaluation of the microphysical processes. *Quarterly Journal of the Royal Meteorological Society*, *123*, 1227–1282.

Rotstayn, L. D., Ryan, B. F., & Katzfey, J. J. (2000). A scheme for calculation of the liquid fraction in mixed-phase stratiform clouds in large-scale models. *Monthly Weather Review*, *128*, 1070–1088.

Salzmann, M., Ming, Y., Golaz, J. C., Ginoux, P. A., Morrison, H., Gettelman, A., et al. (2010). Two-moment bulk stratiform cloud microphysics in the GFDL AM3 GCM: Description, evaluation, and sensitivity tests. *Atmospheric Chemistry and Physics*, *10*, 8037–8064.

Sant, V., Posselt, R., & Lohmann, U. (2015). Prognostic precipitation with three liquid water classes in the ECHAM5–HAM GCM. *Atmospheric Chemistry and Physics*, *15*, 8717–8738.

Sato, Y., Goto, D., Michibata, T., Suzuki, K., Takemura, T., Tomita, H., & Nakajima, T. (2018). Aerosol effects on cloud water amounts were successfully simulated by a global cloud-system resolving model. *Nature Communications*, *9*, 985.

Seifert, A., & Beheng, K. D. (2006). A two-moment cloud microphysics parameterization for mixed-phase clouds. Part 1: Model description. *Meteorology and Atmospheric Physics*, *92*, 45–66.

Seinfeld, J. H., Bretherton, C., Carslaw, K. S., Coe, H., DeMott, P. J., Dunlea, E. J., et al. (2016). Improving our fundamental understanding of the role of aerosol cloud interactions in the climate system. *Proceedings of the National Academy of Sciences*, *113*, 5781–5790.

Sekiguchi, M., & Nakajima, T. (2008). A *k*-distribution-based radiation code and its computational optimization for an atmospheric general circulation model. *Journal of Quantitative Spectroscopy and Radiative Transfer*, *109*, 2779–2793.

Sherwood, S. C., Bony, S., & Dufresne, J.-L. (2014). Spread in model climate sensitivity traced to atmospheric convective mixing. *Nature*, *505*, 37–42.

Song, H., Zhang, Z., Ma, P. L., Ghan, S., & Wang, M. (2018a). The importance of considering sub-grid cloud variability when using satellite observations to evaluate the cloud and precipitation simulations in climate models. *Geoscientific Model Development*, *11*, 3147–3158.

Song, H., Zhang, Z., Ma, P. L., Ghan, S. J., & Wang, M. (2018b). An evaluation of marine boundary layer cloud property simulations in the Community Atmosphere Model using satellite observations: Conventional subgrid parameterization versus CLUBB. *Journal of Climate*, *31*, 2299–2320.

Sorooshian, A., Feingold, G., Lebsock, M. D., Jiang, H., & Stephens, G. L. (2009). On the precipitation susceptibility of clouds to aerosol perturbations. *Geophysical Research Letters*, *36*, L13803. https://doi.org/10.1029/2009GL038993

Staniforth, A., & Cote, J. (1991). Semi-Lagrangian integration schemes for atmospheric models—A review. *Monthly Weather Review*, *119*, 2206–2223.

Stephens, G. L., & L'Ecuyer, T. (2015). The Earth's energy balance. *Atmospheric Research*, *166*, 195–203.

Stephens, G. L., L'Ecuyer, T., Forbes, R., Gettlemen, A., Golaz, J.-C., Bodas-Salcedo, A., et al. (2010). Dreary state of precipitation in global models. *Journal of Geophysical Research*, *115*, D24211. https://doi.org/10.1029/2010JD014532

Stephens, G. L., Li, J., Wild, M., Clayson, C. A., Loeb, N., Kato, S., et al. (2012). An update on Earth's energy balance in light of the latest global observations. *Nature Geoscience*, *5*, 691–696.

Stephens, G. L., Vane, D. G., Tanelli, S., Im, E., Durden, S., Rokey, M., et al. (2008). CloudSat mission: Performance and early science after the first year of operation. *Journal of Geophysical Research*, *113*, D00A18. https://doi.org/10.1029/2008JD009982

Stevens, B. (2015). Rethinking the lower bound on aerosol radiative forcing. *Journal of Climate*, *28*, 4794–4819.
Stevens, B., & Feingold, G. (2009). Untangling aerosol effects on clouds and precipitation in a buffered system. *Nature*, *461*, 607–613.
Sud, Y. C., Lee, D., Oreopoulos, L., Barahona, D., Nenes, a., & Suarez, M. J. (2013). Performance of McRAS-AC in the GEOS-5 AGCM: Aerosol-cloud-microphysics, precipitation, cloud radiative effects, and circulation. *Geoscientific Model Development*, *6*, 57–79.
Suzuki, K., Golaz, J.-C., & Stephens, G. L. (2013b). Evaluating cloud tuning in a climate model with satellite observations. *Geophysical Research Letters*, *40*, 4464–4468. https://doi.org/10.1002/grl.50874
Suzuki, K., & Stephens, G. L. (2009). Relationship between radar reflectivity and the time scale of warm rain formation in a global cloud-resolving model. *Atmospheric Research*, *92*, 411–419.
Suzuki, K., Stephens, G., Bodas-Salcedo, A., Wang, M., Golaz, J.-C., Yokohata, T., & Koshiro, T. (2015). Evaluation of the warm rain formation process in global models with satellite observations. *Journal of the Atmospheric Sciences*, *72*, 3996–4014.
Suzuki, K., Stephens, G. L., & Lebsock, M. D. (2013a). Aerosol effect on the warm rain formation process: Satellite observations and modeling. *Journal of Geophysical Research: Atmospheres*, *118*, 170–184. https://doi.org/10.1002/jgrd.50043
Suzuki, K., Stephens, G. L., van den Heever, S. C., & Nakajima, T. Y. (2011). Diagnosis of the warm rain process in cloud-resolving models using joint CloudSat and MODIS observations. *Journal of the Atmospheric Sciences*, *68*, 2655–2670.
Swales, D. J., Pincus, R., & Bodas-Salcedo, A. (2018). The Cloud Feedback Model Intercomparison Project Observational Simulator Package: Version 2. *Geoscientific Model Development*, *11*, 77–81.
Takahashi, H., Lebsock, M., Suzuki, K., Stephens, G., & Wang, M. (2017). An investigation of microphysics and subgrid-scale variability in warm-rain clouds using the A-Train observations and a multiscale modeling framework. *Journal of Geophysical Research: Atmospheres*, *122*, 7493–7504. https://doi.org/10.1002/2016JD026404
Takemura, T., Egashira, M., Matsuzawa, K., Ichijo, H., O'ishi, R., & Abe-Ouchi, a. (2009). A simulation of the global distribution and radiative forcing of soil dust aerosols at the Last Glacial Maximum. *Atmospheric Chemistry and Physics*, *9*, 3061–3073.
Takemura, T., Nakajima, T., Dubovik, O., Holben, B. N., & Kinne, S. (2002). Single-scattering albedo and radiative forcing of various aerosol species with a global three-dimensional model. *Journal of Climate*, *15*, 333–352.
Takemura, T., Nozawa, T., Emori, S., Nakajima, T. Y., & Nakajima, T. (2005). Simulation of climate response to aerosol direct and indirect effects with aerosol transport-radiation model. *Journal of Geophysical Research*, *110*, D02202. https://doi.org/10.1029/2004JD005029
Takemura, T., Okamoto, H., Maruyama, Y., Numaguti, A., Higurashi, A., & Nakajima, T. (2000). Global three-dimensional simulation of aerosol optical thickness distribution of various origins. *Journal of Geophysical Research*, *105*, 17853.
Tan, I., Strelvmo, T., & Zelinka, M. D. (2016). Observational constraints on mixed-phase clouds imply higher climate sensitivity. *Science*, *352*, 224–227.
Tanelli, S., Durden, S. L., Im, E., Pak, K. S., Reinke, D. G., Partain, P., et al. (2008). CloudSat's cloud profiling radar after two years in orbit: Performance, calibration, and processing. *IEEE Transactions on Geoscience and Remote Sensing*, *46*, 3560–3573.
Tatebe, H., Ogura, T., Nitta, T., Komuro, Y., Ogochi, K., Takemura, T., et al. (2019). Description and basic evaluation of simulated mean state, internal variability, and climate sensitivity in MIROC6. *Geoscientific Model Development Discussion*. https://doi.org/10.5194/gmd-2018-155
Tripoli, G. J., & Cotton, W. R. (1980). A numerical investigation of several factors contributing to the observed variable intensity of deep convection over south Florida. *Journal of Applied Meteorology*, *19*, 1037–1063.
Turner, S., Brenguier, J. L., & Lac, C. (2012). A subgrid parameterization scheme for precipitation. *Geoscientific Model Development*, *5*, 499–521.
Twomey, S. (1977). The influence of pollution on the shortwave albedo of clouds. *Journal of the Atmospheric Sciences*, *34*, 1149–1152.
Ulbrich, C. W. (1983). Natural variations in the analytical form of the raindrop size distribution. *Journal of climate and applied meteorology*, *22*, 1764–1775.
VanZanten, M. C., Stevens, B., Vali, G., & Lenschow, D. H. (2005). Observations of drizzle in nocturnal marine stratocumulus. *Journal of the Atmospheric Sciences*, *62*, 88–106.
Waliser, D. E., Li, J. L. F., L'Ecuyer, T. S., & Chen, W. T. (2011). The impact of precipitating ice and snow on the radiation balance in global climate models. *Geophysical Research Letters*, *38*, L06802. https://doi.org/10.1029/2010GL046478
Waliser, D. E., Li, J. L. F., Woods, C. P., Austin, R. T., Bacmeister, J., Chern, J., et al. (2009). Cloud ice: A climate model challenge with signs and expectations of progress. *Journal of Geophysical Research*, *114*, D00A21. https://doi.org/10.1029/2008JD010015
Walters, D. N., Best, M. J., Bushell, A. C., Copsey, D., Edwards, J. M., Falloon, P. D., et al. (2011). The Met Office unified model global atmosphere 3.0/3.1 and JULES global land 3.0/3.1 configurations. *Geoscientific Model Development*, *4*, 919–941.
Wang, J., Daum, P. H., Yum, S. S., Liu, Y., Senum, G. I., Lu, M. L., et al. (2009). Observations of marine stratocumulus microphysics and implications for processes controlling droplet spectra: Results from the marine stratus/stratocumulus experiment. *Journal of Geophysical Research*, *114*, D18210. https://doi.org/10.1029/2008JD011035
Wang, Z., French, J., Vali, G., Wechsler, P., Haimov, S., Rodi, A., et al. (2012). Single aircraft integration of remote sensing and in situ sampling for the study of cloud microphysics and dynamics. *Bulletin of the American Meteorological Society*, *93*, 653–668.
Wang, M., Ghan, S., Liu, X., L'Ecuyer, T. S., Zhang, K., Morrison, H., et al. (2012). Constraining cloud lifetime effects of aerosols using A-Train satellite observations. *Geophysical Research Letters*, *39*, L15709. https://doi.org/10.1029/2012GL052204
Wang, M., Ghan, S., Ovchinnikov, M., Liu, X., Easter, R., Kassianov, E., et al. (2011). Aerosol indirect effects in a multi-scale aerosol-climate model PNNL-MMF. *Atmospheric Chemistry and Physics*, *11*, 5431–5455.
Watanabe, M., Emori, S., Satoh, M., & Miura, H. (2009). A PDF-based hybrid prognostic cloud scheme for general circulation models. *Climate Dynamics*, *33*, 795–816.
Wentz, F. J., Hilburn, K. A., & Smith, D. K. (2012). Remote sensing systems DMSP SSMIS monthly environmental suite on 0.25 deg grid, version 7. Remote Sensing Systems, Santa Rosa, CA. Available online at www.remss.com/missions/ssmi.
Wilson, D. R., & Ballard, S. P. (1999). A microphysically based precipitation scheme for the UK Meteorological Office unified model. *Quarterly Journal of the Royal Meteorological Society*, *125*, 1607–1636.
Wood, R. (2005a). Drizzle in stratiform boundary layer clouds. Part I: Vertical and horizontal structure. *Journal of the Atmospheric Sciences*, *62*, 3011–3033.
Wood, R. (2005b). Drizzle in stratiform boundary layer clouds. Part II: Microphysical aspects. *Journal of the Atmospheric Sciences*, *62*(1969), 3034–3050.
Wood, R. (2012). Stratocumulus clouds. *Monthly Weather Review*, *140*, 2373–2423.
Wood, R., & Hartmann, D. L. (2006). Spatial variability of liquid water path in marine low cloud: The importance of mesoscale cellular convection. *Journal of Climate*, *19*, 1748–1764.
Wood, R., Mechoso, C. R., Bretherton, C. S., Weller, R. A., Huebert, B., Straneo, F., et al. (2011). The VAMOS ocean-cloud-atmosphere-land study regional experiment (VOCALS-REx): Goals, platforms, and field operations. *Atmospheric Chemistry and Physics*, *11*, 627–654.

Wu, P., Dong, X., & Xi, B. (2015). Marine boundary layer drizzle properties and their impact on cloud property retrieval. *Atmospheric Measurement Techniques*, *8*, 3555–3562.

Wu, P., Xi, B., Dong, X., & Zhang, Z. (2018). Evaluation of autoconversion and accretion enhancement factors in general circulation model warm-rain parameterizations using ground-based measurements over the Azores. *Atmospheric Chemistry and Physics*, *18*, 17405–17420.

Xiao, F., Okazaki, T., & Satoh, M. (2003). An accurate semi-Lagrangian scheme for raindrop sedimentation. *Monthly weather review*, *131*(5), 974–983.

Yang, P., Bi, L., Baum, B. A., Liou, K.-N., Kattawar, G. W., Mishchenko, M. I., & Cole, B. (2013). Spectrally consistent scattering, absorption, and polarization properties of atmospheric ice crystals at wavelengths from 0.2 to 100 μm. *Journal of the Atmospheric Sciences*, *70*, 330–347.

Zhang, Z., Ackerman, A. S., Feingold, G., Platnick, S., Pincus, R., & Xue, H. (2012). Effects of cloud horizontal inhomogeneity and drizzle on remote sensing of cloud droplet effective radius: Case studies based on large-eddy simulations. *Journal of Geophysical Research*, *117*, D19208. https://doi.org/10.1029/2012JD017655

Zhang, S., Wang, M., Ghan, S. J., Ding, A., Wang, H., Zhang, K., et al. (2016). On the characteristics of aerosol indirect effect based on dynamic regimes in global climate models. *Atmospheric Chemistry and Physics*, *16*, 2765–2783.

Zhao, X., Lin, Y., Peng, Y., Wang, B., Morrison, H., & Gettelman, A. (2017). A single ice approach using varying ice particle properties in global climate model microphysics. *Journal of Advances in Modeling Earth Systems*, *9*, 2138–2157. https://doi.org/10.1002/2017MS000952

Zhou, C., & Penner, J. E. (2017). Why do GCMs overestimate the aerosol cloud lifetime effect? A comparison of CAM5 and a CRM. *Atmospheric Chemistry and Physics*, *17*, 21–29.